2017

The Consequences of a Reduced Superlattice Thickness on Quantum Cascade LASER Performance

Pedro Figueiredo
University of Central Florida

THE CONSEQUENCES OF A REDUCED SUPERLATTICE THICKNESS ON QUANTUM CASCADE LASER PERFORMANCE

by

PEDRO NORMAN FIGUEIREDO
Bachelor of Science, University of Central Florida, 2011

A dissertation submitted in partial fulfillment of the requirements
for the degree of Doctor of Philosophy
in the Department of Physics
in the College of Science
at the University of Central Florida
Orlando, Florida

Spring Term
2017

Major Professor: Arkadiy Lyakh

ABSTRACT

Coherent infrared radiation sources are essential for the operability of a wide range of scientific, industrial, military and commercial systems. The importance of the mid-infrared spectral region cannot be understated. Numerous molecules have some vibrational band in this range, allowing for identification of species by means of absorption, emission or some other form of spectroscopy. As such, spectroscopy alone has numerous applications ranging from industrial process control to disease diagnosis utilizing breath analysis. However, despite the discovery of the LASER in the 60s, to this day the amount of coherent sources in this range is limited. It is for this reason that the quantum cascade laser has gained such momentum over the past 23 years.

Quantum Cascade LASERS (QCL) are semiconductor LASERS which are based on the principle of bandgap engineering. This incredible technique is a testament to the technological maturity of the semiconductor industry. It has been demonstrated that by having precise control of individual material composition (band gap control), thicknesses on the order of monolayers, and doping levels for each individual layer in a superlattice, we have unprecedented flexibility in designing a LASER or detector in the infrared. And although the technology has matured since it's discovery, there still remain fundamental limitations on device performance. In particular, active region overheating limits QCL performance in a high duty cycle mode of operation.

In this dissertation, along with general discussion on the background of the QCL, we propose a solution of where by limiting the growth of the superlattice to a fraction of typical devices, we allow for reduction of the average superlattice temperature under full operational conditions. The consequences of this reduction are explored in theory, experiment and system level applications.

ACKNOWLEDGMENTS

Throughout my PhD I have had the opportunity to participate in a host of projects and had the pleasure of working with many colleagues. Below is a short acknowledgement for their assistance during this era of my life.

I would like to thank my advisor, Dr. Arkadiy Lyakh for allowing me to work under his supervision during the last of my PhD at the University of Central Florida. During a time of uncertainty in the program, he stepped in and provided the necessary funding for myself to complete the program with a topic that I had longed to be granted funding to pursue. Without his deep knowledge and patience, I would have not been able to finish this work.

I would also like to thank Dr. Robert Peale, Dr. Richard Klemm, and Dr. Sasan Fathpour for serving on my dissertation committee and evaluating this dissertation. Throughout the years, Dr Peale has served as a figure whom I could consult with on many programs which I was apart and submitted for.

Although no related research is presented here, I would extend a thank you to Dr. James Ginn, Dr. David Shelton, Dr Glenn Boreman from Plasmonics Inc, for allowing me to further my skills within the cleanroom and research setting.

I would also extend gratitude towards Mr Guy Zummo, for what fraction of his vast technical expertise was imparted upon me during his stay at the university. In addition, thanks to my colleagues Mathew Suttinger for his assistance with COMSOL thermal simulations, Ankesh Todi for his assistance with setting up various experiments, and Rowel Go for his assistance with testing devices.

I would also thank Dr. Ahmed Halawany, Ashutosh Rao, Dr. Farnood Rezaie, Dr. Deep Panjwani, Alex Dillard, Dr Andrew Warren, Edward Dean, Dr. Ivan Divliansky, Seth Colhoun, Dr. Janardan Nath, Dr. Jose Garcia, Marcin Malinowski, Dr. Evan Smith, Chris Frederickson, Dr Imen Rezadad, Daniel Franklin, Joshua Perlstein and many other of my friends and colleagues not mentioned here for consultation or assistance during cleanroom fabrication runs and testing.

I would like to thank my family for their constant love, support and encouragement through this engagement.

Above all, I would like to express my deepest gratitude to my wife, Jacqueline. Thank you for standing beside me through this daunting time in my life and putting up with me through many late nights and days apart. You have given me the motivation to complete this program.

to my wife, my brother, my mother, and my father

TABLE OF CONTENTS

LIST OF FIGURES

LIST OF TABLES

LIST OF ABBREVATIONS

AOM – Acoustic Optic Modulator

fs - femtosecond

IR – infrared

km – kilometer

LWIR – long-wave infrared

m- meter

MIR – mid-wave infrared

mm - millimeter

ms – millisecond

nm – nanometer

pm – picometer

ps – picosecond

QCL – Quantum Cascade Laser

s – second

THz – terahertz

µm – micrometer

CHAPTER 1: INTRODUCTION TO THE INFRARED

1.1. Introduction

Light is an oscillating electro-magnetic field exhibiting wave-like and particle-like properties. In vacuum, also commonly referred to as free space, the speed at which light travels is measured to be (c~300km/ms). The speed at which light propagates through space (v) depends on certain properties of the propagation media but can be represented as a function known as the index of refraction of that media (n). The wave property of light dictates that the frequency (f) at which light propagates through a media is inversely proportional to its wavelength (λ) multiplied by its speed or $= v/\lambda = (c \cdot n)/\lambda$. We categorize light according to its wavelength. Table 1-1 shows the various names of bands of light.

Table 1-1 :Electromagnetic Spectrum classification as a function of free space wavelength

Gamma Rays	<10pm
X-Ray	10pm – 10nm
UltraViolet	10nm – 400nm
Visible	400nm – 700nm
Infrared	700nm – 1mm
Microwave	1mm – 1m
Radio	>1m

The band of radiation that this thesis focuses is the Infrared. Since William Herschel first discovered the radiation in 1800 [1], countless scientific works have been published utilizing suites of engineering marvels to produce or observe infrared radiation. Infrared radiation may be further sub-classified into five bandwidths depending on division scheme. For the purpose of this work, we utilize the common terminology in dealing with infrared devices as shown in Table 1-2.

Table 1-2 Sub division of Infrared portion of the Electromagnetic Spectrum based upon common detectors

Near Infrared	0.7µm-1.0µm
Short-Wave Infrared	1.0µm-3µm
Mid-Wave Infrared	3µm-8µm
Long Wave Infrared	8µm-12µm
Very Long Wave Infrared	12µm – 30µm
Far Infrared	30µm-1000µm

Research into this field over the following century led to the work of Rayleigh, Wien and Planck, among others, in developing the theory of blackbody radiation, which describes the phenomenon of self-radiation. All charged particles, including atoms, will oscillate and emit electromagnetic radiation at a specific frequency or wavelength. The amount of radiant energy an object emits, and the frequencies at which it emits that energy, depends on its temperature and emissivity. This is known as blackbody radiation or thermal radiation and obeys Plank's distribution.

1.2. Introduction to LASERS

Unlike thermal radiation, LASER radiation is a quantum mechanical effect that is exploited to obtain radiation. The radiation distribution may widely vary depending on the type of LASER. A LASER is an acronym used to describe devices which have the property of stimulated emission. In particular LASER stands for light amplification by stimulated emission of radiation.

As previously mentioned, lasers are widely varying in design but all have the same core elements and operate on the same principle. In that a large amount of energetic particles are pumped from their rest state (lower level) into an excited state known as the upper level. When this occurs, there exists a probability that the particle will spontaneously de-energize itself to a lower energy state by the emission of a quanta of light known as a photon. The frequency of this light is directly proportional to the energy difference between these upper and lower energy levels. If a photon interacts with a particle on the upper laser level, the particle will emit a photon of the same phase

and direction. This is the principle of stimulated emission. However, if a photon interacts with a particle on the lower laser level, that photon will be absorbed and the particle will transition to the upper laser level. It is for this reason that the 2 level system needs to be pumped such that there exists more particles in the upper laser level than the lower laser level. This is the concept of population inversion. [2]

Although there exists many different LASERs in existence today, we focus on solid state semiconductor lasers in this thesis. In particular, a relatively new addition to the LASER world, the intersubband laser known as the quantum cascade LASER.

1.3. Outline of This Dissertation

This dissertation focuses on the effects and applications of limiting the growth thickness of the superlattice of a quantum cascade LASER designed around 5.6μm to a fraction of typical devices. The subsequent chapters of this dissertation are organized in the following manner:

- Chapter 2: Discussion on the basics of defining the Quantum Cascade LASER
- Chapter3: MicroFabrication techniques utilized to create a Quantum Cascade LASER
- Chapter4: Discussion and experimental results of a sample grown with the designed superlattice of reduced thickness
- Chapter5: Extension of the reduced thickness material to surface emitting devices
- Chapter6: Application of the material towards an external cavity with wavelength tuning for spectroscopy

CHAPTER 2: BACKGROUND OF QUANTUM CASCADE LASERS

2.1. A Brief History

The Quantum Cascade LASER was first demonstrated at Bell Labs in 1994 [3]. Although its invention was first conceived by Capasso (1986), the movement towards the unipolar LASER can be argued to have started in 1960 with Lax's proposed [4] semiconductor optical transitions utilizing same band transitions between Fermi levels. Due to the discovery of the GaAs diode LASER produced in 1962 by Hall at General Electric [5], much research focus was diverted from a unipolar device to a band-gap based one in an effort to be the first group to demonstrate continuous wave operation at room temperature. No major technological research on a unipolar device was published until 1971 by Kazarinov and Suris [6]; a year after room temperature continuous wave operation had been reached for the diode LASER demonstrated by Bell labs [7] and the Ioffe Institute [8] independently. The proposed device by Kazarinov and Suris, suggested that optical gain was achievable from an electrically biased super lattice of two-dimensional quantum states. This revolutionary idea allowed for emission wavelengths to engineered from material growth thicknesses as opposed to being bound by the material property of band-gaps.

"The Quantum Cascade Laser make us finally free from the bandgap slavery" - Cappasso [9]

The core technology that was essential for the quantum cascade laser to have come into existence is owed to epitaxial growth pioneered by Arthur and Cho in 1968. This thin film deposition technique to grow crystalline material with no crystalline defects and atomic level precision was essential to produce the hundreds of quantized states necessary to produce a quantum cascade laser. These varying thin films have well defined interfaces and are lattice matched allowing for electronic transport between differing layers with minimal interactions other than a change in

potential and effective mass. Because of the lack of crystalline defects, the in plane wave-vector is decoupled from the out-of plane wavevector, allowing epitaxial system to be spatially quantized dictated by quantum mechanics.

Since Faist first demonstrated it in ’94, the quantum cascade laser has evolved as a technology from operating solely at cryogenic temperature in the mid-wave to operation at room temperature from the mid-infrared to the long wave regime. Demonstrations at the terahertz regime have also been demonstrated at cryogenic temperatures. Further milestones to the quantum cascade laser technology have included obtaining watt-level operation at room temperature, wall plug efficiencies exceeding 28% [10], and broadband devices exceeding 500 wavenumbers [11]. Although much of the technology has been matured, there still remains further research opportunities for progressing the technology including but not limited to; operation in the near infrared, room temperature operation in the terahertz, and increased power output.

2.2. The Basics of the Quantum Cascade LASER

The Quantum Cascade LASER is a semiconductor device that emits stimulated radiation in the Infrared to the terahertz. QCLs exploit the phenomena known as intersubband transitions observed when a material dimension is on the order of the DeBroglie wavelength of an electron. At these dimensions electrons may transition between confined states of the same band. As a consequence, the energy required to transition between different states is much smaller than an interband transitions, allowing for various non-radiative scattering mechanisms to limit the electron lifetime to the order of pico-seconds.

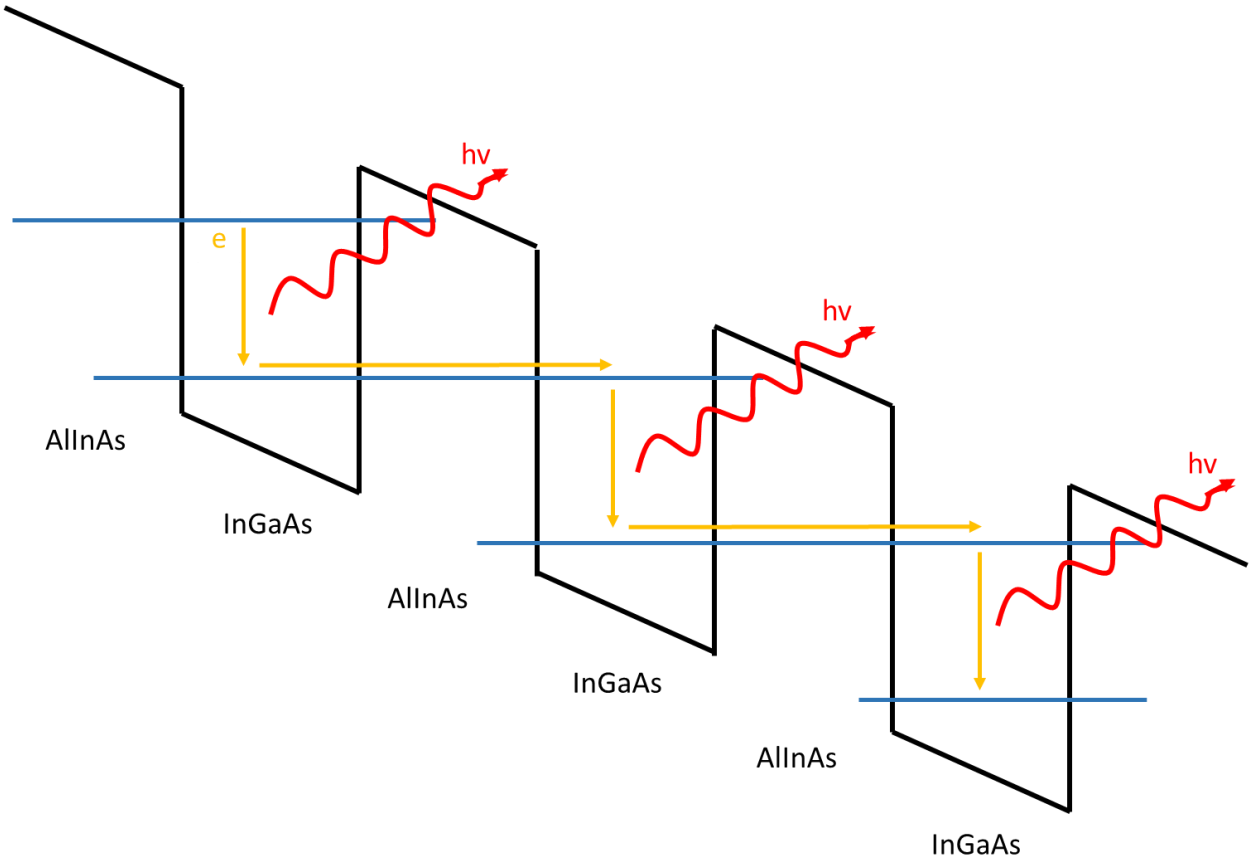

Figure 2–1: Representative diagram of varying quantum wells and barriers illustrating intersubband cascading effect.

This size-quantized confinement allows the electronic states to be modeled by the classical quantum mechanical particle in a box problem; see appendix A for details. As varying materials are grown, the bandgap energies of the grown materials dictate the barrier heights and well depths, while the thickness determines the barrier and well dimensions as shown in Figure 2–1. If the barrier thicknesses are thin enough, quantum states of individual wells may couple with one another allowing for electrons to tunnel between various wells and transition to various energy levels within the neighboring wells. This coupling is illustrated in figure 2-2 for a 5 quantum well structure of lattice matched AlInAs and InGaAs with barriers of 100A and 10A.

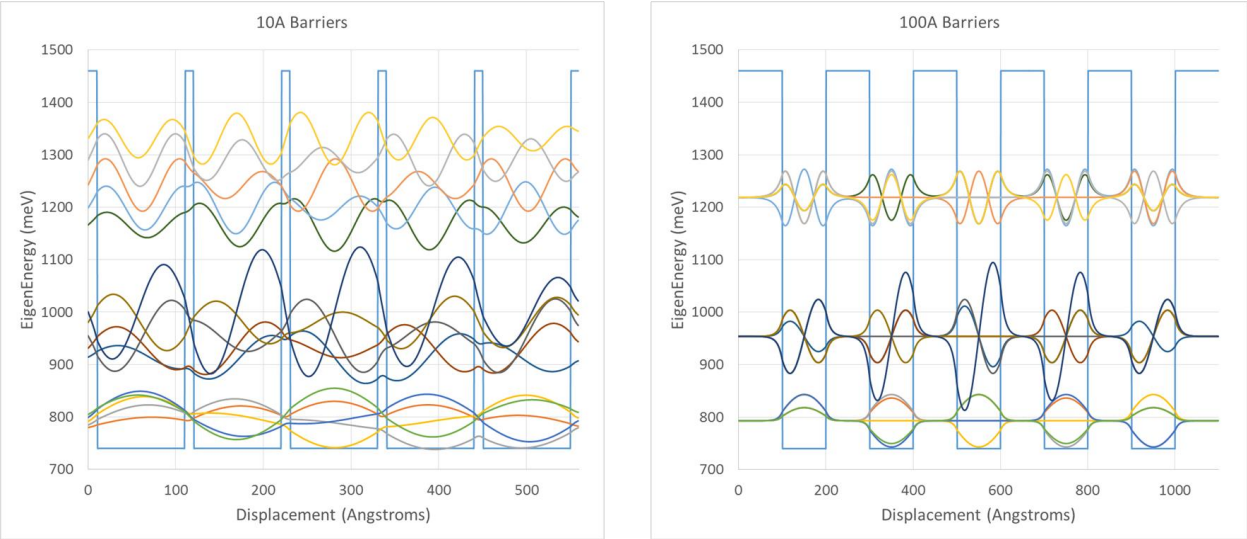

Figure 2–2: Numerical solutions to multi quantum well problem utilizing the shooting method discussed in appendix A.

In this manner radiative transitions become possible to engineer. This unipolar device may be further engineered to have a particular set of repeating wells and barriers, known as a stage, repeated multiple times to have a single electron to be recycled multiple times in a cascading like regime to output multiple photons.

2.3. The structure of the superlattice

Key to the success of a QCL structure is the demonstration of the structure 1) being electrically stable at operating voltage; 2) achieving population inversion at operating voltage; 3) Gain should be larger than loss. The superlattice design of a Quantum cascade LASER may be broken into two distinct regions each with their own unique purpose. Each critical to the successful operability of a QCL device. Figure 2-3 illustrates these structure regions.

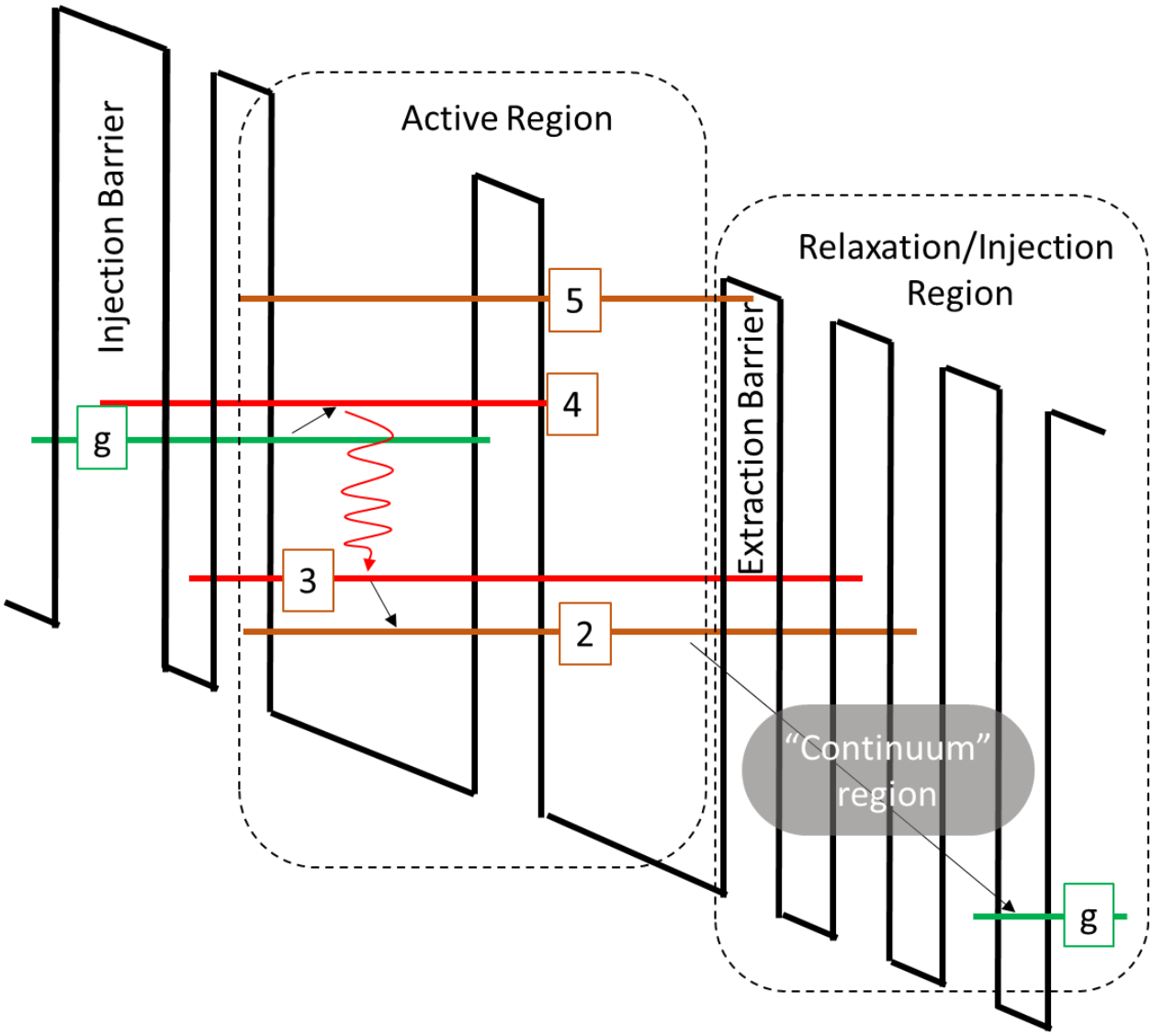

Figure 2–3: Schematic of conduction band superlattice diagram of quantum cascade LASER. Typical primary eigenstates and regions in a superlattice.

The active region is the primary region designed for output of photons. Electrons from the ground state are injected into the upper LASER state 4 where by electrons accumulate for stimulated emission and radiatively transfer to the lower LASER state 3. In order to quickly depopulate state 3, state 2 is energetically distanced from state 3 at the LO phonon resonance energy; such that the lifetime of state 2 is smaller than the lifetime of state 3 ($\tau_3 > \tau_2$). Electrons then enter the relaxation region where by its main purpose is to depopulate state 2 and create resonant tunneling to the upper

LASER wave state of the next cascaded stage. This is accomplished by a series of wavefunctions that are densely populated in what is known as the continuum region. Additional function of the relaxation region is to 1) prevent the formation of electrical domains; 2) increase the separation of lower LASER state 2 and the ground state for injection of the next stage to minimize thermal backfill; 3) Assist with minimizing electron scattering into parasitic state 5 which allows electrons to bypass the upper laser level 4.

2.4. Predicting Laser performance

A typical quantum cascade laser's optical power vs current curve is displayed in Figure 2–4. There are three distinct values which characterize performance:

1. Threshold current (J_{th}) – Current required for lasing to begin
2. Slope efficiency (dp/dI) – Amount of output power as a function of current
3. Maximum current (J_{max}) – Maximum amount of current supported by the device

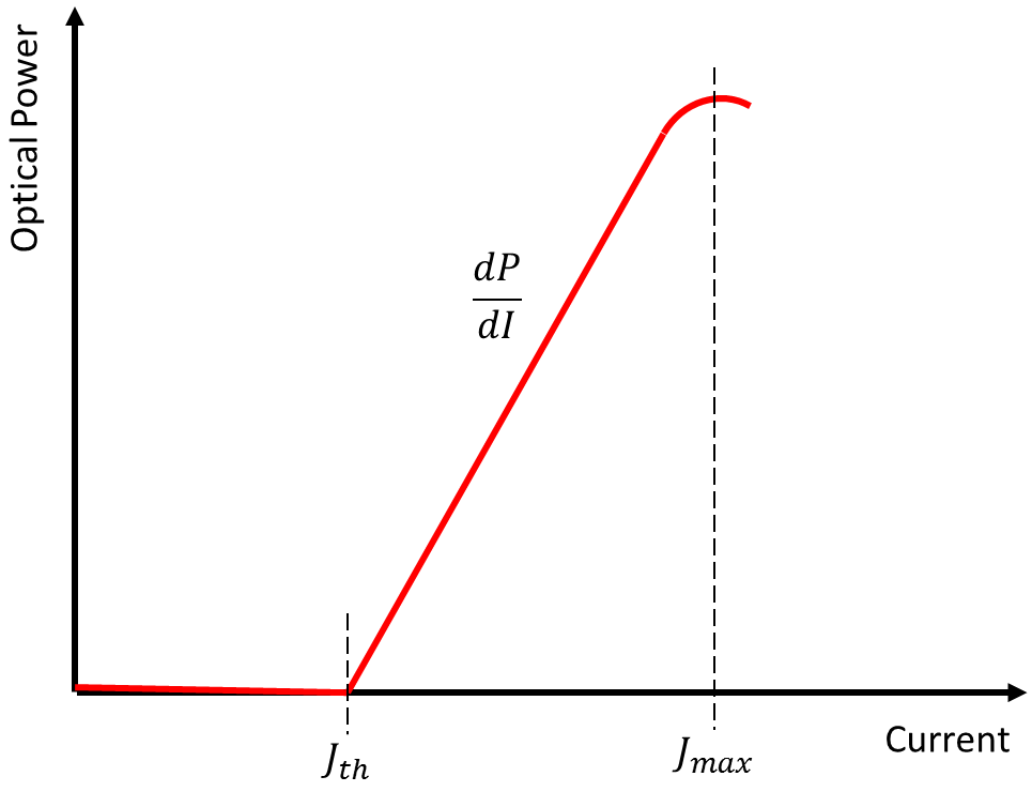

Figure 2–4: Schematic of typical Power vs Current (LI) curve for a quantum cascade laser

Determination of the threshold current and slope efficiency depends on transport within the active region of figure 2-3 and can be described by a rate equation model [12]. For simplicity we consider a three state system corresponding to states 4, 3 and 2 of figure 2-3. We also assume that the injector state has a constant electron population denoted by n_g and injects electrons into state 4 at a rate equal to the current density divided by the fundamental electron charge; J/e. We also allow electrons to transition from state 4 to states 2, 3 and the continuum; denoted by τ_{42}, τ_{43}, τ_{escape} respectively. Life times of states 2 and 3 are denoted as τ_2, τ_3. We also allow for electrons to be thermally activated to state 3 to a thermal equilibrium population, $n_3^{thermal}$. The rate of change of electron population in states 4 and 3 are given by.

$$\frac{dn_4}{dt} = \frac{J}{e} - \frac{n_4}{\tau_4} - S \cdot g_c \cdot (n_4 - n_3) \tag{2-1}$$

$$\frac{dn_3}{dt} = \frac{n_4}{\tau_{43}} + S \cdot g_c \cdot (n_4 - n_3) - \frac{(n_3 - n_3{}^{thermal})}{\tau_2} \tag{2-2}$$

And the rate of change of photon flux density (S) is given by

$$\frac{dS}{dt} = \frac{c}{n} \cdot (S \cdot (g_c \cdot (n_4 - n_3) - \alpha_{total} - ß\frac{n_3}{\tau_{sp}}) \tag{2-3}$$

Where α_{total} is the total waveguide loss for the cavity, ß is the fraction of spontaneous emission coupled into the lasing mode, τ_{sp} is the lifetime of spontaneous emission, n is the refractive index. The gain cross section g_c is directly proportional to the mode overlap factor Γ, the dipole matrix element z_{43}, and inversely proportional to the wavelength λ, the cavity length L, and the transition broadening γ_{43} given as

$$g_c = \Gamma \frac{4 \cdot \pi \cdot e^2 {z_{43}}^2}{2 \cdot \varepsilon_0 \cdot n \cdot \lambda \cdot \gamma_{43} L} \tag{2-4}$$

In the sub-threshold condition the electron populations on each state are presumed to be in steady state and no photons are emitted such that equations 2-1, 2-2 and S are equivalently zero. Solving for population of states n_4 and n_3 and taking the difference yields the population inversion. When the population inversion multiplied by the gain cross section is equivalent to the total modal losses, threshold current (J_{th}) is found and given as

$$J_{th} = \frac{e}{(1 - \tau_3/\tau_{43})} \cdot (\frac{\alpha_{tot}}{g_c} + {n_3}^{thermal}) \tag{2-5}$$

Examining equation 2-5, we directly observe that the threshold current is dependent on two terms. The first term depends proportionally on the waveguide loss and the inverse of the gain cross section. In design of the superlattice, by maximizing the overlap between states 4 and 3 to increase the dipole matrix element, a reduction of threshold is observed. To minimize the second term of thermal backfill into state two, $n_3{}^{thermal}$ a large voltage offset is needed between the

ground state of the next stage and state 3. This is typically accomplished by designing the QCL to either operate at high voltages or increasing the number of layers within the relaxation/injection region. The target energy separation for most designs is 4x~6x larger that k·T at room temperature. Alternatively, operation of the device at cryogenic temperature will reduce k·T, minimizing the voltage offset required for reducing thermal backfill.

In a similar fashion we can also solve for slope efficiency given as

$$\frac{dP}{dI} = N_p \frac{hv}{e} \frac{\alpha_m}{\alpha_{total}} \frac{\tau_4}{\tau_4+\tau_3} \tag{2-6}$$

The slope efficiency is directly dependent on the number of stages and inversely proportional to mirror losses.

The maximum current supported by the device can be calculated utilizing a density matrix approach given in [12] and is given as

$$J_{max} = \frac{en_s\Omega^2\tau_{||}}{1+4\Omega^2\tau_{||}\tau_3} \tag{2-7}$$

The total output power of the device is then given as the difference of the maximum current and threshold current multiplied by the slope efficiency. By design, we have control over all variables in Equation 2-7 less the $\tau_{||}$ which is the decoherence time between the ground state of the injector and the upper laser level. To increase the maximum current supported by the device, the coupling between the injection state and the upper laser state should be maximized, or alternatively the sheet density increased.

CHAPTER 3: FABRICATION OF THE QUANTUM CASCADE LASER

3.1. Introduction

As mentioned previously, it is due to the advent of the semiconductor technology that allowed the idea of the Quantum Cascade LASER to come into existence. The feat of the quantum cascade laser is a true testament to the maturity of the tools and technologies developed by the semiconductor transistor field allowing for the realization of quantized confinement. Without the advances in this field, the quantum cascade laser may not have existed.

Standard semiconductor techniques to fabricate the quantum cascade LASER may be broken down into the following processing segments.

1. Epitaxial Growth
2. Waveguide Formation
3. Electrical Contacts
4. Die Formation

3.2 Epitaxial Growth

Critical to the formation of the quantum cascade LASER lies a thin film deposition technique as mentioned before. This technique is known as epitaxial growth and produces films that continue the crystalline state of a single crystalline wafer. The deposited film has spatial coherence over large distances due to lack of crystalline defects and purity of the deposited material. Currently two competing techniques exist for the production of epitaxial films.

The molecular beam epitaxy system in general is a physical vapor deposition chamber. Key properties of the system are outlined below.

- High vacuum capabilities with base pressures less than 10^{-10} torr.
- Extreme cleanliness to ensure purity of the deposition
- Wafer substrate heating capability
- Temporal accuracy of mechanical shutters
- High Purity evaporant sources loaded in a Knudsen cell

At its core, the molecular beam epitaxy system is essentially a highly sophisticated thermal evaporator. Cells containing the evaporants are heated to vapor points where due to the low chamber pressure, mean free path is orders of magnitude larger than atmospheric pressure allowing the particle to travel to the substrate. Once the vapor reaches the substrate, its energy is adsorbed by the wafer and over time many particles create a thin film. To control thickness, actuating shutters allow the gaseous phase of the material to travel to the substrate for an allotted time associated with a deposition rate; typically on the order of Angstroms per second.

The other epitaxy system is known as the metal-organic chemical vapor deposition chamber. The working principle is similar to a traditional chemical vapor deposition with the exception that the gaseous precursors are composed typically of hydrides of group V and organometalics of group III. A carrier gas flows with the gas precursors and based on the ratio between flow rates of different gasses thermal decomposition favors crystalline growth on a heated III-V wafer substrate. Time is utilized to vary film thicknesses.

Once an engineered design is set, the design is implemented and grown with one of the two deposition techniques with waveguide cladding layers grown before and after depending on the operating wavelength designed. A typical active region is displayed in Figure 3–1.

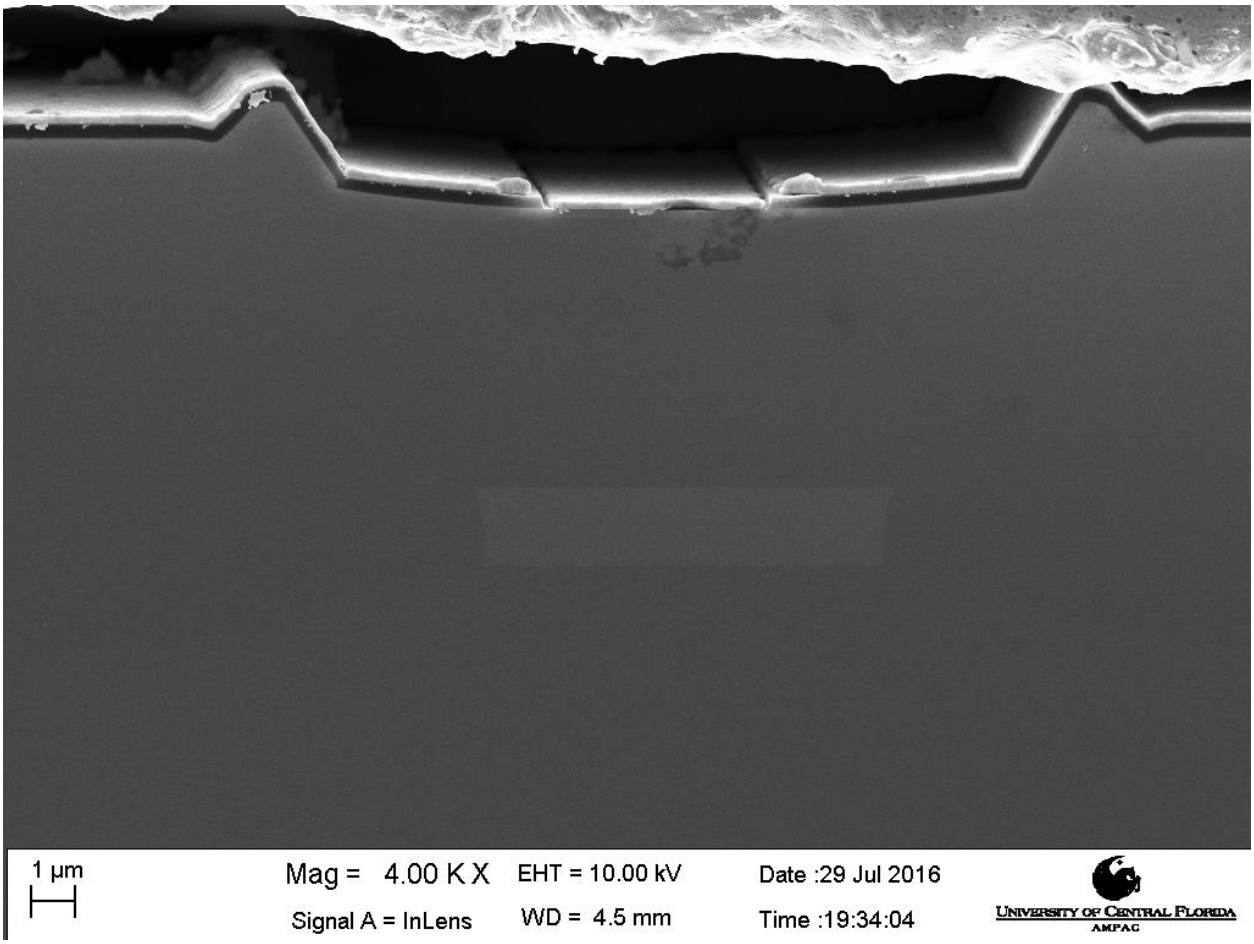

Figure 3–1: Scanning electron microscope image of a cross sections active region of varying quantum wells (InGaAs) and quantum barriers (InAlAs)

3.3 Waveguide formation

Once the material is grown it becomes necessary to create an optical cavity for lasing to occur. Due to thermal constraints of intersubband devices, there lies a power limitation limiting the lateral dimensions of the waveguide typically to the order of tens of microns in width. For a typical edge emitting device the waveguide is formed following the standard semiconductor techniques below. Additionally, due to the high costs associated with epitaxially grown films, particularly within an

academic environment, wafers are typically cleaved to smaller dimensions on the order of cm^2 to be processed in an effort to conserve material.

The epitaxial wafer is initially cleaned with acetone and isopropanol to remove any residual organics that may have deposited on the surface over time. A positive photoresist is deposited by a spin coat method to achieve a uniform thickness across the wafer. In order to set the resist, the sample is exposed to heat at 110C for 1minute to remove solvent from the spin. A contact lithography mask utilized within a contact lithography system is placed over the mask and aligned to the crystal plane of the wafer. The photoresist is then exposed to ultraviolet radiation, which transfers the ridge mask pattern into the resist. The resist is then exposed to a developer that selectively removes areas that were exposed by ultraviolet radiation. The sample is then mounted to a microscope slide utilizing a small amount of photoresist acting as an adhesive and is baked for an additional 3minutes. The sample is then exposed to an oxygen plasma to remove any residual polymer that may not have fully washed in the developer bath.

Thickness of the resist is initially measured with a profilometer. A hydrobromic and nitric acid solution diluted with deionized water is prepared having a 1:1:10 part respectively. Holding the sample vertically, the sample is inserted into the solution and agitated in a back/forth motion to assist with obtaining a more anisotropic etch. The etchant solution readily reacts with III-V based materials and does not interact with the photoresist allowing the patterned area to be transferred into the epitaxial material. After 100 seconds the sample is submerged into deionized water and dried with nitrogen. A secondary thickness measurement is ran and the difference between the first measurement is calculated to obtain the depth achieved and a removal rate is calculated. Prior knowledge of the grown structure is needed in order to know at what depth the “active” lasing epitaxial portion is. The etch is continued until the active region is laterally confined across the

sample in order to limit lasing output to single mode, reduce the amount of heat generated and to limit the current requirements of the device. Since quantum cascade lasers are unipolar devices, the creation of midgap states at the lateral interface by this etch does not influence laser performance. Confirmation of the etch depth is conducted with the profilometer before the sample is cleaned with acetone, isopropyl alcohol and an oxygen plasma to remove the photoresist mask.

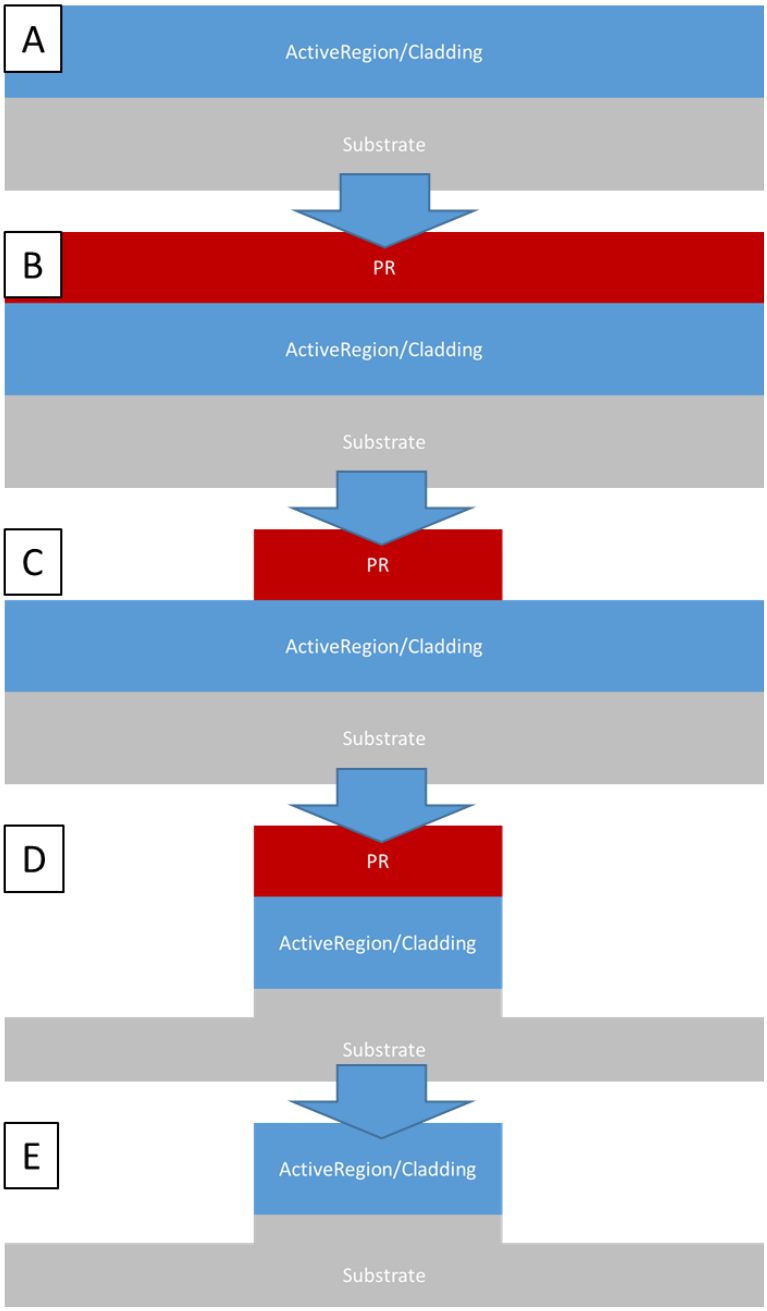

Figure 3–2: Processing steps for ridge formation. A) Wafer with epitaxial material is cleaved and cleaned. B) Photoresist is spun coat. C) Photoresist is exposed and developed leaving stripe pattern D) Utilizing the photoresist as a wet etch mask the sample is submerged into a HBr:HNO3 solution E) Photoresist is stripped and the sample is cleaned.

3.4 Electrical Contacts

We now provide contacts to only the portion of the sample where the mode is confined. To do this, the sample is submerged into a hydrofluoric, ammonium fluoride and deionized water 1:1:6 part solution to prepare the surface for electrical insulation deposition. A plasma enhanced chemical vapor deposition chamber is utilized for this thin film that is deposited. Chamber conditions are as follows: 800mTorr, 400sccm SiH4, 20sccm NH4, 200Watts of high frequency plasma at a temperature of 300C. Approximately 300nm of insulation material is deposited conformally to the profile of the ridge, preventing lateral injection of current for the future metal layer.

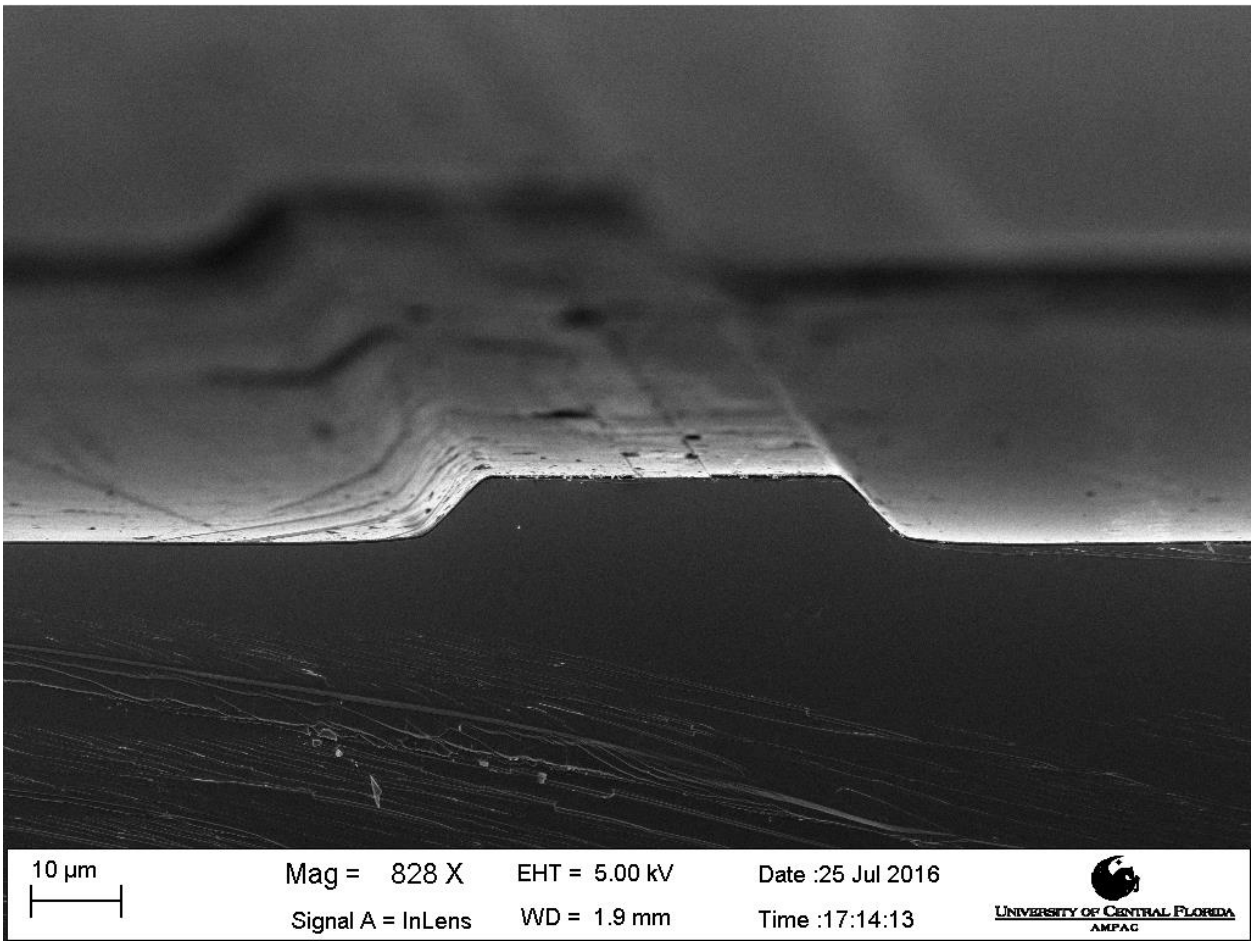

Figure 3–3: Scanning electron microscope image of a cross section of a single ridge wave guide processed to completion

A photoresist mask is applied to the structure and an opening atop of the ridge is developed. This photoresist is then utilized as an etch mask during a selective etch targeted towards the silicon nitride layer utilizing a fluorinated chemistry in a reactive ion etching tool. The following chamber conditions in a UniAxis ICP/RIE: 300mTorr, 50Watts RIE, 200Watts ICP, 20sccm of sulfur hexafluoride. Once the silicon nitride etch is completed, the photoresist mask is stripped utilizing the methods demonstrated above.

Utilizing a physical vapor deposition technique, a thin film of titanium and gold is conformally deposited on the surface creating ohmic contact at the point of injection. The sample is then mounted to a stage utilizing wax and is lapped down to a thickness that is sub 200um, allowing for cleaner cleaving with reduced striations. This is accomplished with an Al2O3 1um grit size on a cloth-like pad. The sample is removed from the mount, cleaned and back side is deposited with germanium and gold contact layer.

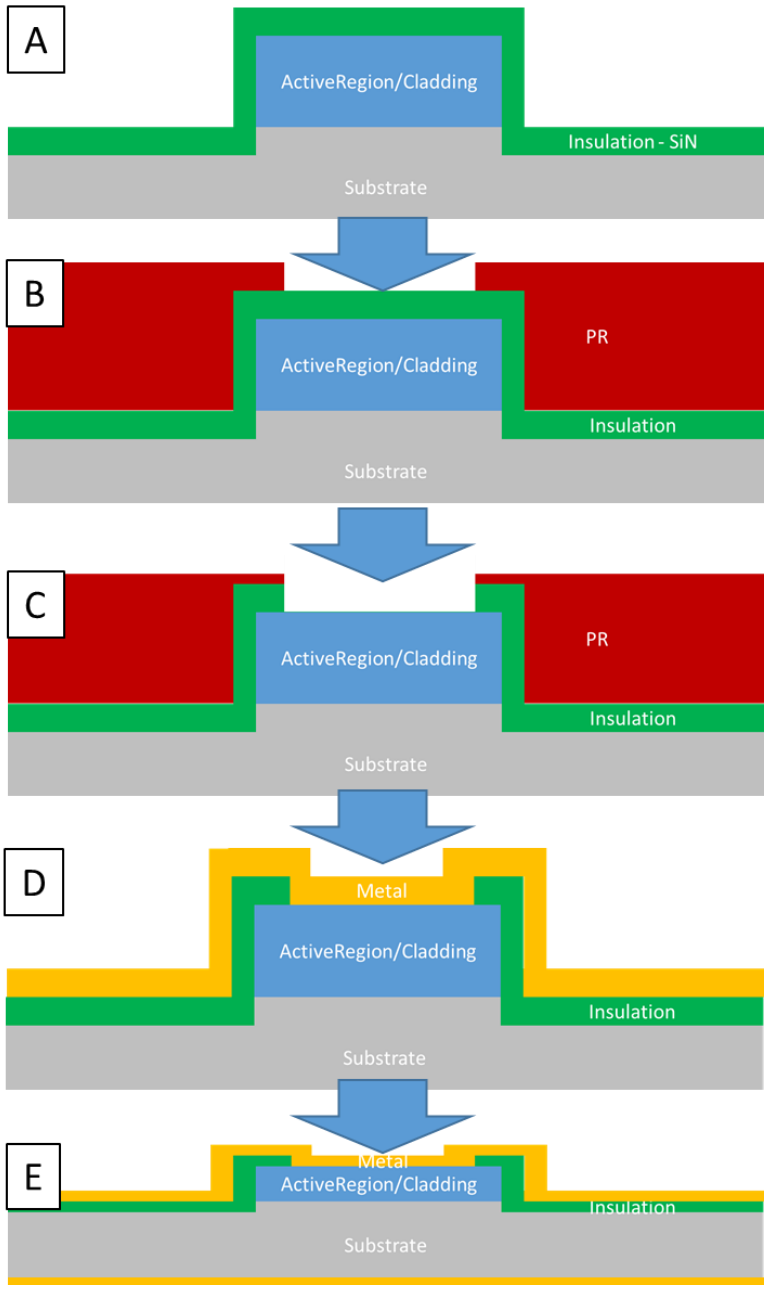

Figure 3–4: Processing steps for electrical contacts A) Sample is coated with Silicon Nitride utilizing decomposition of SiH4 and NH3 in a PECVD. B) Photoresist is spun coat and exposed C) A window is etched into the SiN by exposing the sample to a SF6/O2 plasma within an ICP RIE. D)Ti Au contact layer is deposited by means of a physical vapor deposition chamber E) The sample is polished to a thickness <200µm and backside Ge Au contact layer is deposited by means of a physical vapor deposition chamber

3.5 Die Formation

Once the backside contact is deposited the sample is mounted on a low tack adhesive tape and loaded into a scribe and break tool. Within the tool a diamond scribe with 20um tip is used in conjunction with a microscope and micrometer stage to scribe areas where the die is to be formed. Typically there is one LASER per die. Once scribed, the machine holds the sample in place and applies a backside force to create a two separate pieces along the cleaving crystal plane. This process is repeated perpendicular to the facets to produce clean defect free mirrors to produce a Fabry Perot cavity.

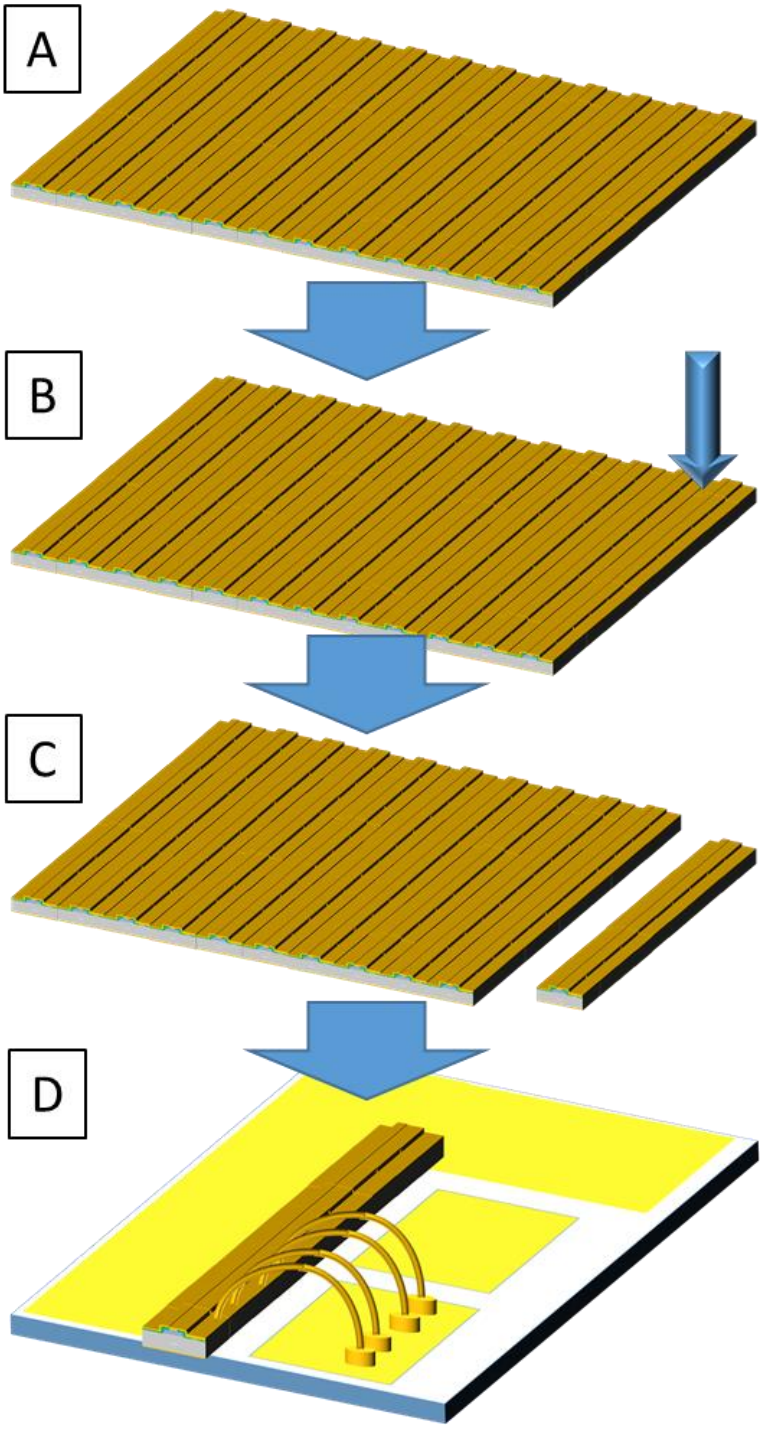

Figure 3–5: Processing steps for die formation and mounting A) Completed sample is cleaned B) a diamond scribe scores a small section of the sample C) An upward pressure propagates the defect along the crystal plane separating the LASER from the rest of the sample. D)LASER chip is bonded to a SnAu alloy submount and contact wirebonds are made allowing for electrical contacts

CHAPTER 4: QUANTUM CASCADE LASERS WITH REDUCED STAGES

4.1. Introduction

One of the main obstacles that still impedes the quantum cascade laser technology is the combination of low growth rates for precision of the epitaxial growth and several cascading stages in the super lattice resulting in the thick active regions. This results in total epi-growth times exceeding several hours resulting in expensive growths and drifts in deposition conditions; leading to gain broadening and lower device performance. This expensive growth alone typically costs about ~2/3 the total cost of a ridge emitting QCL fabrication run as depicted in Figure 4–1.

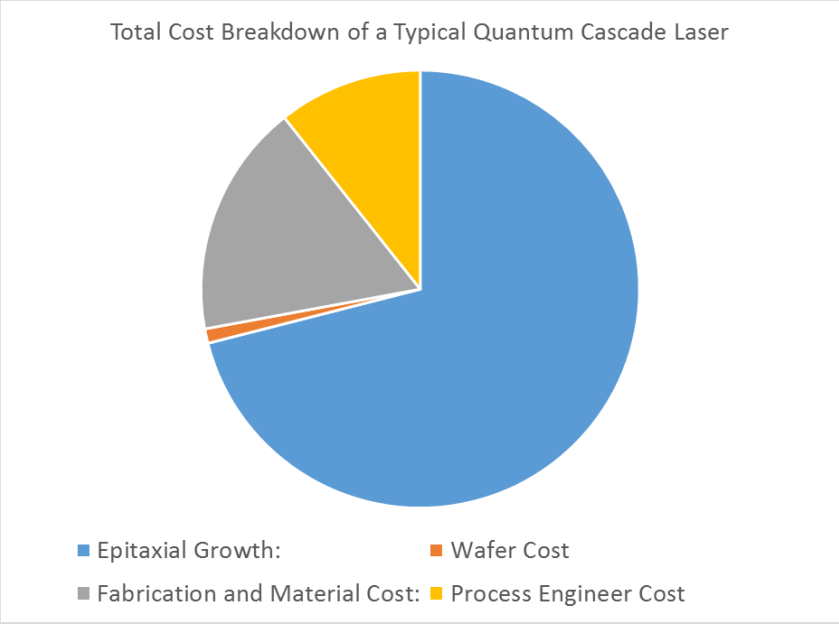

Figure 4–1: Percent cost breakdown of a Quantum Cascade Laser cleanroom fabrication run. Current prices based on quotations recieved from an epi-growth foundry and pricing from the cleanroom facilities in the Central/North Florida region.

A quantum cascade laser with a thinner active region may have a lower variation in active region layers thicknesses and compositions, leading to a higher material gain per stage and sub

sequentially reducing price per deposition. A two to three fold reduction in its thickness would significantly reduce overall epi-growth time as the active region comprising up to 3,000 nanometer-thick layers is typically grown at a rate of (or less than) one angstrom per second in contrast to the epitaxial-growth of the cladding layers which are on a done at a relatively high rate, on a scale of several angstroms per second [13]. The reduction in active region thickness and its impact on laser performance are discussed in this chapter.

4.2. Theoretical Considerations

The quantum cascade laser active region typically comprises thirty to fifty gain stages with each stage designed for one injected electron to efficiently emit one photon. One of the main reasons for using a large number of stages is to increase modal gain and, therefore, reduce laser threshold current density and increase laser dynamic range as previously shown in chapter 2. The latter is defined as difference between maximum (roll over) and threshold current densities. Threshold current density (J_{th}) can be expressed as:

$$J_{th} = J_{tr} + \frac{\alpha_{tot}}{\Gamma \cdot g} \tag{4-1}$$

where J_{tr} stands for transparency current density, αtot - total optical losses, g – differential gain, and Γ – mode overlap factor with the active region, where we have rewritten equation 2-5. Transparency current density is required to reach the transparency condition when carrier populations on the upper and lower laser levels are equal. It is a function of injection efficiency for the upper laser level and carrier backscattering to the lower laser level. As follows from the data presented in [10], transparency current density can account for over 50% of threshold current

density. Since the former is independent of the number of stages, it may not be critical to achieve a large overlap factor and to use a large number of stages in the design of high performance QCLs. When continuous wave (CW) or high duty cycle operation is needed, the configuration with a reduced number of stages offers an additional critical advantage of reduced thermal resistance. The average temperature of the active region, hereby referred to simply as active region temperature, for QCLs can feasibly exceed 400K under full operational conditions [14]. The main reason for laser core overheating is an inherently low thermal conductivity of the ternary semiconductor materials used in the active region design (AlInAs and InGaAs) depicted in Figure 4–2.

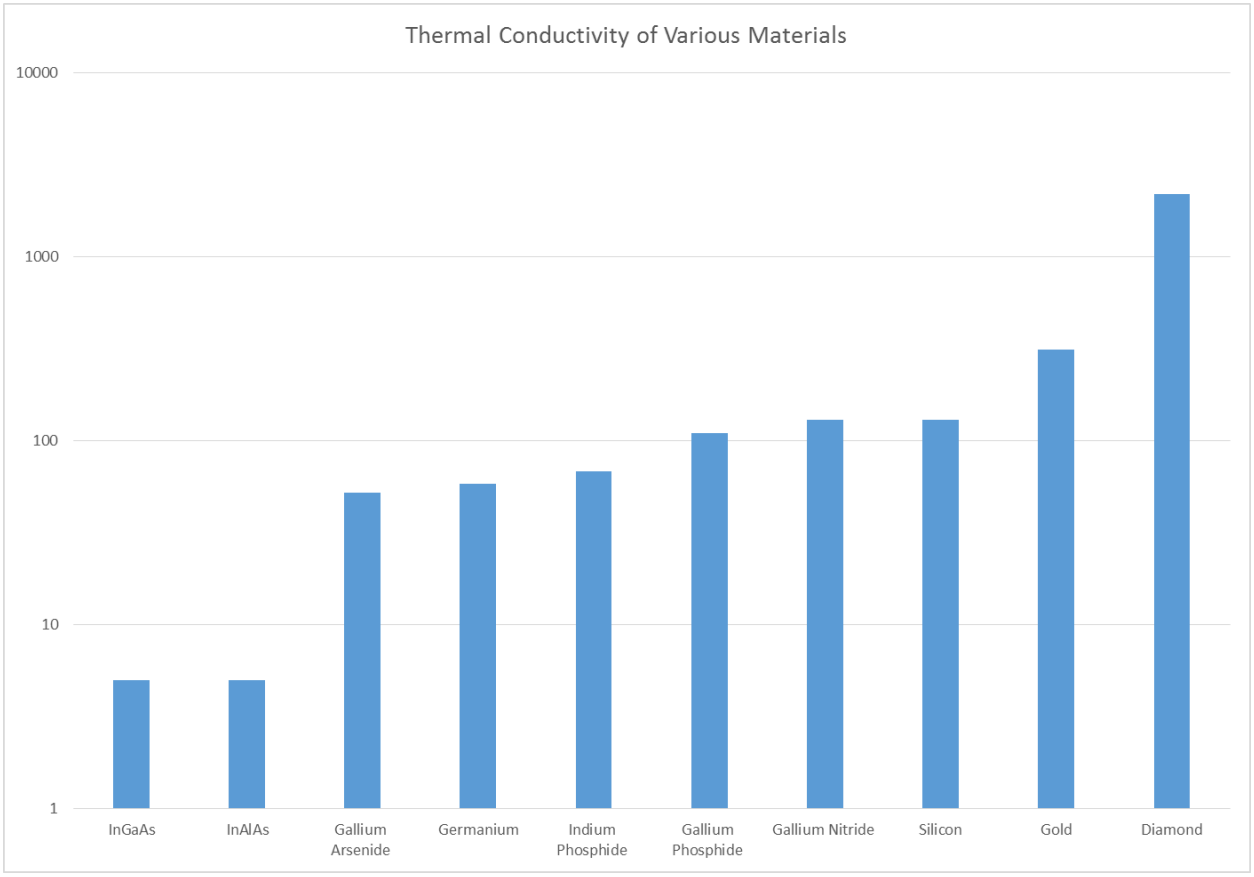

Figure 4–2:Thermal conductivity in units of Watts/m°K for various materials.

Thermal transport is further hindered in the epi-growth direction by the superlattice structure of the active region. Since laser performance reduces as temperature increases, the reduction in laser thermal resistance is one of the main laser design goals. In particular, active region temperature can be reduced by reducing the thickness of the material with the lowest thermal conductivity, i.e. by reducing the active region thickness.

As previously mentioned, due to thermal constraints the lateral dimension of a ridge emitting device is limited. This is especially the case when transitioning the laser from low duty cycle operation to the quasi continuous wave regime, as the device is not given ample time to cool. As such, current methods of increasing the power output is limited to increasing cavity length and not the lateral dimension of the device.

The red solid/dashed curves in Figure 4–3 show that the calculated maximum/average active region temperature increases from 435K/383K to 495K/440K when active region width of a 1.85 μm-thick (40-stage) structure increases from 10 μm to 40 μm. To carry out these calculations, it was assumed that the electrical current density of 3 kA/cm2 was injected into the device under the bias of 16.5 V, which corresponds to the roll-over condition for the exemplary structure. The rapid self-heating of the active region makes it very difficult to efficiently scale CW QCL optical power for the traditional QCL configuration.

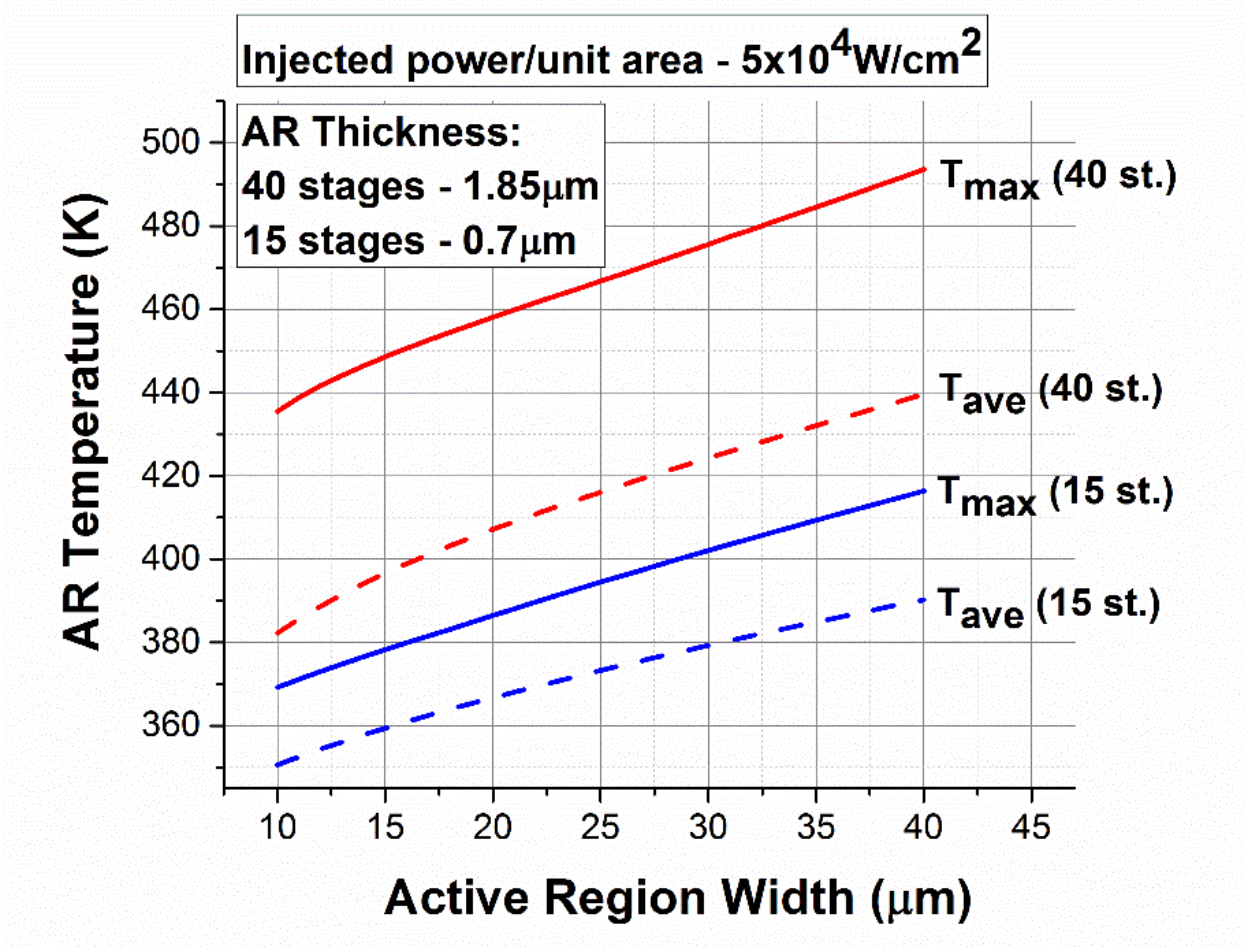

Figure 4–3: Simulated active region (AR) temperature dependence on active region width. Injected power per unit area was kept constant at 5x10^4 W/cm2 for all studied cases. Red curves – 40-stage geometry; blue curves – 15-stage geometry; solid lines – maximum active region temperature (center of the active region); dashed lines – average temperature across the active region.

The blue solid curve in Figure 4–3 demonstrates that for the same electrical power injected per active region unit area, the maximum active region temperature rise for a 0.7 μm-thick, 40 μm-wide structure is projected to be less than that for the 1.85 μm-thick, 10 μm-wide structure. In addition, the difference between the maximum and average temperatures that can be used as a measure of a thermal gradient (and stress) in the active region is only half that for the 40-stage

structure. In other words, it is possible to inject four times larger total electrical power in the thin and wide device without compromising active region temperature. This approach can be used for CW optical power scaling.

Figure 4-3 demonstrates that projected average active region temperature reduces from 380K to 350K when the active region thickness (number of stages) reduces from 1.85μm (40 stages) to 0.7μm (15 stages) for the same total electrical power of 14.4W injected into a 3mm x 10μm BH device. Simulations were done within COMSOL assuming the device is mounted epi-down on an AlN submount, using anisotropic thermal conductivity (1 W/(m·K) along growth direction and 4 W/(m·K) in the epi-layers plane), and using an exemplary injected power density corresponding to the operational point for QCLs reported in [15].

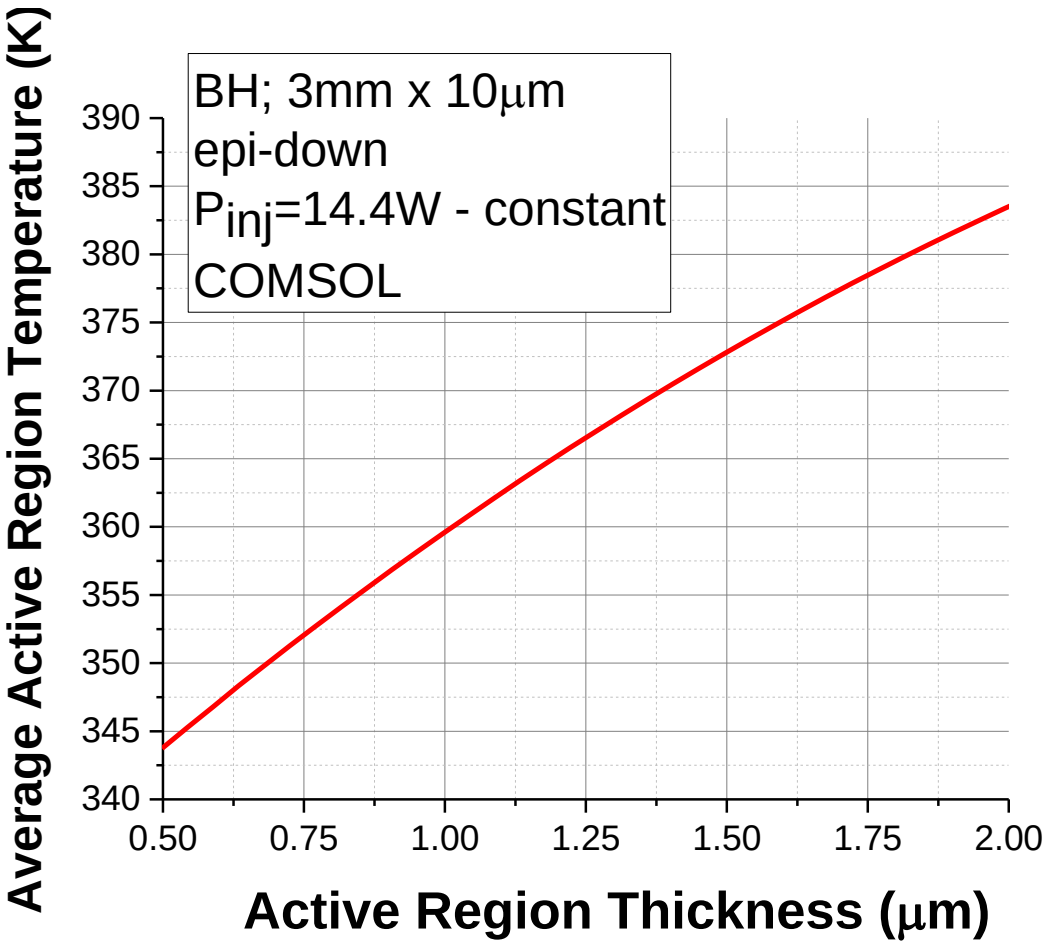

Figure 4–4: Calculated (COMSOL) dependence of average active region temperature on active region thickness for an exemplary QCL design. Total injected electrical power dissipated in the active region was kept constant at 14.4W for changing thickness. Device configuration: buried heterostructure, 3mm x 10μm, epi-down mounted on AlN submount.

Figure 4-4 shows that calculated thermal resistance for an active region with a cross-section of 0.7μm x 10μm (15 stages) is 3.5K/W, much lower than its value of 5.4K/W calculated for devices with 1.85μm x 10μm cross-section (40 stages). As a consequence, average active region temperature of 380K is projected to be reached for this configuration when total injected electrical power exceeds 23W, a value that is significantly higher than 14.4W calculated for the 40-stage structure. As discussed above and experimentally shown below, QCL pulsed efficiency does not change dramatically with a change in number of stages. Therefore, counterintuitively, due to a

larger range of injected power density allowed in CW operation, QCLs with a reduced number of stages can produce CW optical power comparable to that for their traditional "thick active region" counterparts with the same cavity length.

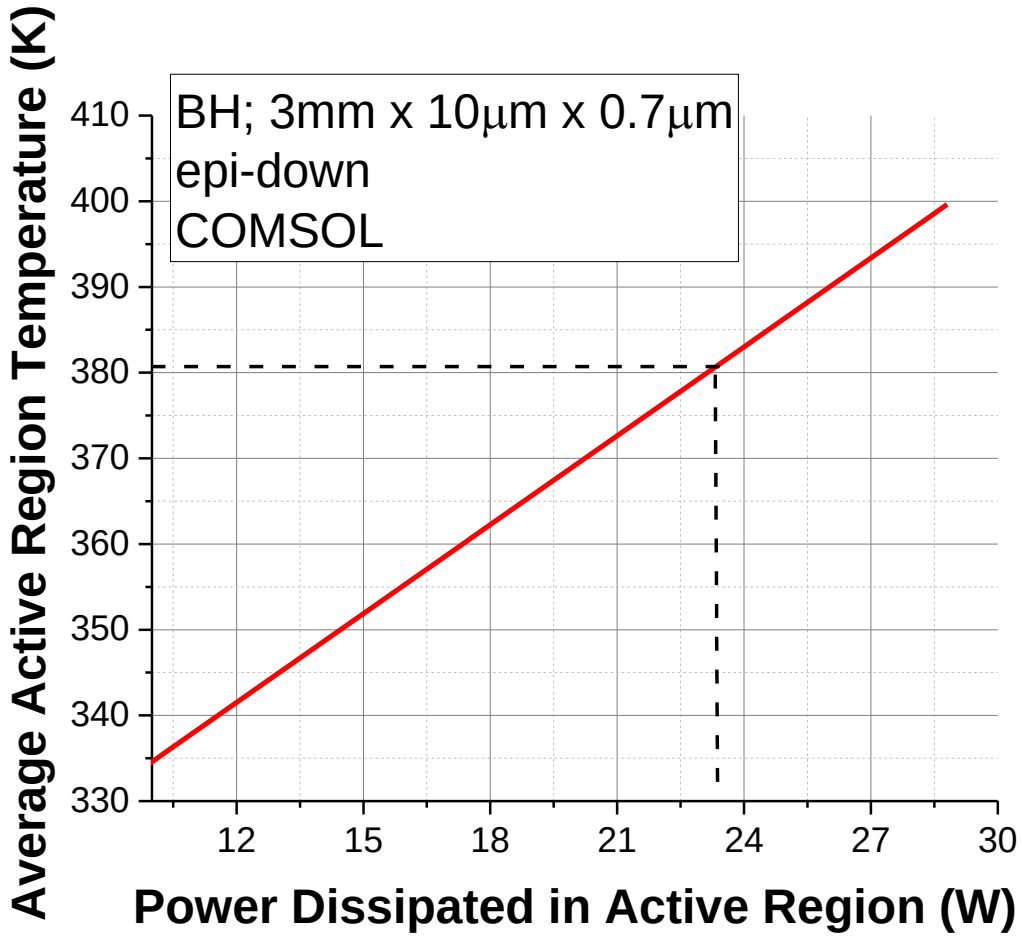

Figure 4–5: Calculated (COMSOL) dependence of average active region temperature on power dissipated in the active region for a 15-stage design. Device configuration: buried heterostructure, 3mm x 10μm x 0.7μm, epi-down mounted on AlN submount. Corresponding thermal resistance for the 15-stage design is 3.5K/W vs. 5.4K/W for a 40-stage design.

The reduction in a number of active region stages proportionally reduces laser slope efficiency [15]. Therefore, to achieve a high optical power level, a structure with a reduced number of stages should be designed to have an increased laser dynamic range. This can be achieved through a combination of an increased active region/injector coupling and an increased active region doping.

The structure reported in [10] was optimized for a high peak power, high pulsed efficiency operation. It had the maximum current density of approximately 9 kA/cm2, two to three times larger than that for state-of-the-art CW structures. The combination of the high maximum current density and the very high efficiency makes that design suitable for the present study.

4.3. Results and Discussion

A 15-stage structure with the active region and waveguide designs reported in [10] has been grown by molecular beam epitaxy and then processed into the traditional BH configuration. The reduction in active region thickness resulted into ~40% reduction in growth time. Laser chips were subsequently cleaved from the wafer and mounted epi-down on AlN submounts.

Figure 5-3 shows pulsed and CW optical power vs. current and voltage vs. current characteristics for a 2.1 mm by 10 μm device with a high reflection (HR) coated back facet and an uncoated front facet. CW curves were measured only up to 1.6A due to a limited current range of the CW laser current driver.

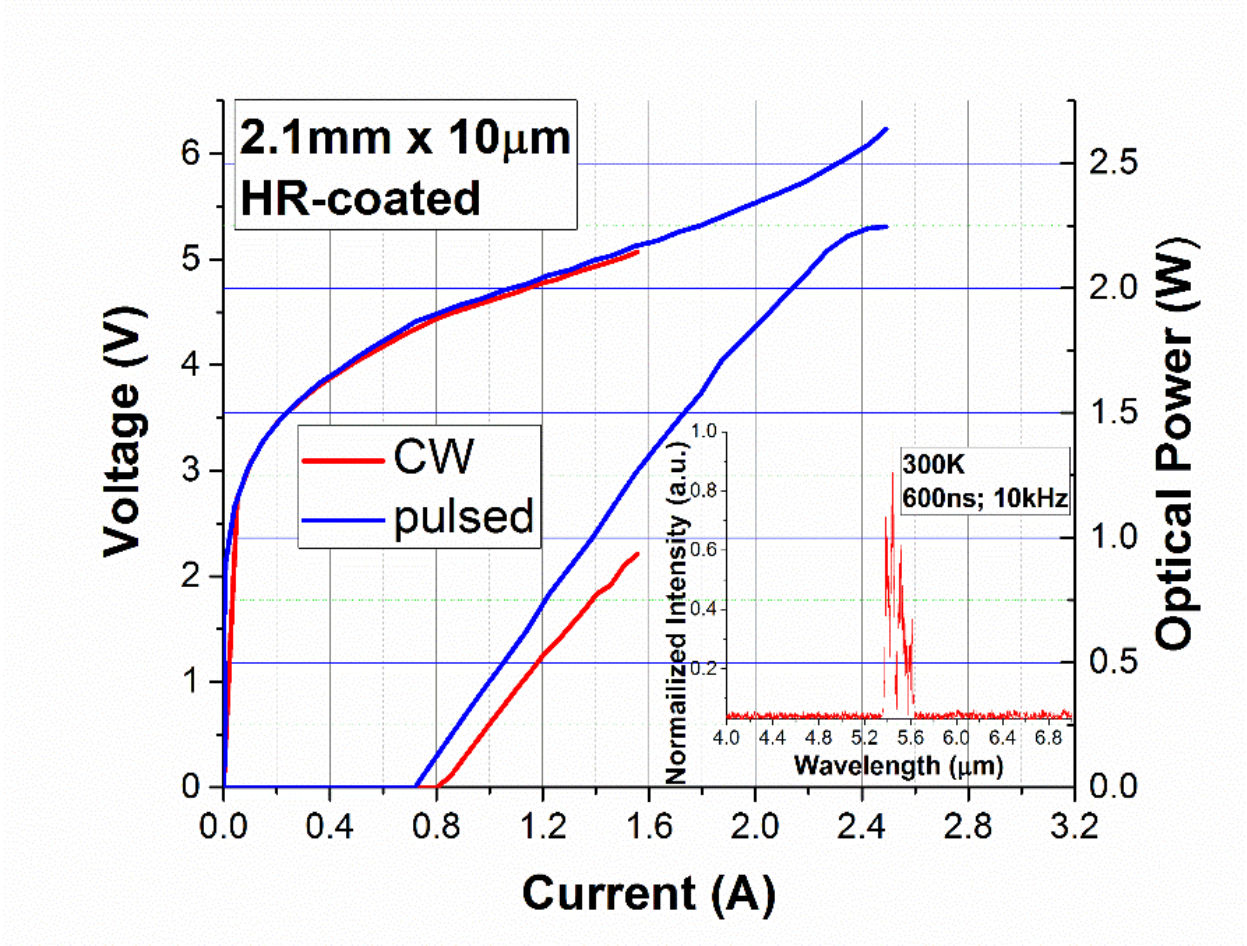

Figure 4–6: Pulsed (600ns; 10kHz) and CW optical power vs. current and voltage vs current characteristics measured for a HR-coated 2 mm x 10 μm QCL at 293K. The inset shows that the laser spectrum is centered at 5.55 μm.

The measured pulsed slope efficiency of 0.10W/A per stage was very close to that for 40-stage devices with the same mirror losses [15]. Corresponding pulsed threshold current density and maximum current density were measured to be 3.1 kA/cm2 and 11.9 kA/cm2, respectively. Roll over voltage was 6.2V, which is 0.62V higher than its value projected based on the 40-stage structure data. The latter result suggests that there is an additional series resistance for the 15-stage structure and that laser performance can be further improved if the series resistance is reduced.

Measured CW slope efficiency in the vicinity of laser threshold was found to be 1.42W/A, very close to its pulsed value of 1.45W/A. At the same time, CW threshold current density was measured to be 3.7 kA/cm2, higher than its pulse-mode value of 3.1kA/cm2. The comparison between CW and pulsed data for slope efficiency and threshold current density results are generally consistent with the large T1 and a relatively low T0 values measured for this design in [10]. If we compare the output power of this device to a high output device as in [15], which has a linear power density of .45W/mm as compared to the 15 stage structure having linear power density larger than 0.5W/mm; we see the advantage of the reduction of number of stages. This power density is expected to increase as we increase lateral dimensions of the device.

Maximum measured wall plug efficiency in pulsed and CW modes of operation was 18% and 12%, respectively. Note that if the series resistance problem for the 15-stage structure is resolved, corresponding efficiency values are projected to increase to approximately 20% and 14%. Therefore, the projected pulsed efficiency for the 15-stage structure is only 25-30% lower than its value for the reference 40-stage design. This is despite the fact that mode overlap factor is 3.5 times lower for the "thin active region" structure as shown in Figure 4–7. These experimental data demonstrate that laser efficiency does has a relatively weak dependence on number of stages.

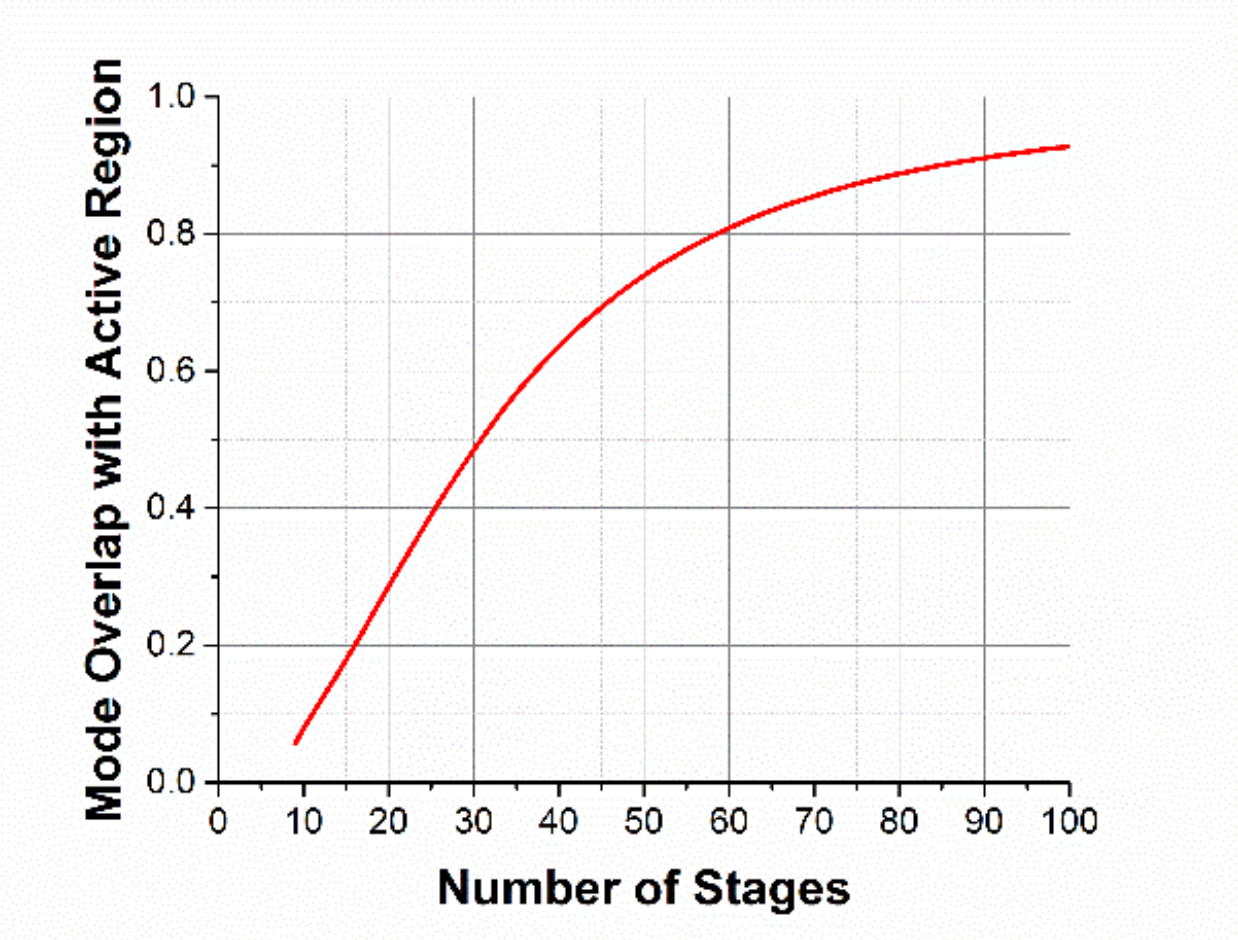

Figure 4–7: Calculated (COMSOL) mode overlap factor dependence on number of QCL stages for the structure reported in Ref. 5-2.

QCL optical power can be approximately scaled with cavity length by optimizing output facet reflectivity [16]. Therefore, the value of optical power normalized to the active region footprint can be used to evaluate high power capability of a particular design and can be compared across different structures. In the case of CW QCLs, such comparison results depend on injected electrical power, laser efficiency, and laser thermal resistance. The significantly reduced thermal resistance for the 15-stage design allows for CW operation at much higher injected power density, three to four times higher than that for traditional designs reported in [15] and [17]. As a consequence, the normalized power level for the new design with active region is high. Figure 4–3 shows that the

15-stage structure is capable of producing over 0.5W of CW power per 1mm of cavity length in the 10μm-wide BH configuration. This power level is comparable to that for the 40-stage structure reported in [15] and exceeds that for the structure reported in [17]. The data demonstrates that the QCL configuration with a reduced number of stages is suitable for high-power applications. Also, these results are very promising for the development of high power broad area QCLs [18] as they show that a combination of a low thermal resistance and high optical power/high performance required for power scaling with the lateral device dimension (ridge width) is possible.

Threshold current density and slope efficiency dependence on laser cavity length measurements (1/L method) were performed for the 15-stage structure and compared to corresponding values for the reference 40-stage design. 72% injection efficiency ηi extracted from the data was close to its value of 75% measured in [10]. Measured change in Γ·g from 5.4cm/kA for the 40-stage structure to 2.2 cm/kA for the 15-stage structure can be explained by the corresponding reduction in Γ (Figure 4–7). Finally, waveguide losses of 0.80 cm-1 measured for the 15-stage design differed from 1.2 cm-1 losses measured for the 40-stage design also due to the difference in mode overlap factor with the active region.

The comparison between waveguide losses for the two designs allows to separate total waveguide losses into the active region losses α_{AR} and losses originating from the cladding layers α_{cl}. Total waveguide losses can be represented as

$$\alpha_w = (1 - \Gamma)\cdot \alpha_{cl} + \Gamma \cdot \alpha_{AR} \qquad (4\text{-}2)$$

Based on Eq. 2, the combination of the measured values for αw and the calculated values for Γ yields α_{cl} = 0.7 cm-1 and α_{AR} = 1.4 cm-1. These results show that the intersubband losses have a significantly larger contribution to overall waveguide losses than the free carrier losses and that intersubband losses should be minimized in the QCL design.

The experimentally obtained values for $(1-\Gamma)\cdot\alpha_{cl}$ are in a good agreement with the values calculated based on the classical Drude model. Experimental/model data for cladding losses for the 40-stage design are 0.25cm-1/0.14cm-1 and for the 15-stage design – 0.56cm-1/0.39cm-1. The higher value of α_{cl} for the 15-stage design is due to a larger mode overlap with the outer cladding layers that have a higher doping level. The discrepancy between the model and experimental data likely stems from an uncertainty in the carrier scattering time used in the classical Drude model [19] (its typical range for QCL structures is from 100 to 200fs).

CHAPTER 5: SURFACE EMISSION OF A BESSEL BEAM

5.1. Introduction

For many system level applications, there exists a requirement for an array of devices to produce different power or color output on a spatial dependence such as infrared scene generation or hyperspectral imagers. When considering a system incorporating an array of devices, system level performance is dependent on isolation between devices of the array. As previously mentioned, systems incorporating quantum cascade lasers will have to mitigate the large amount of heat produced from a single device. That is, heat produced from one device will affect neighboring devices, limiting operating temperature conditions and degradading lasing and overall device performance. Thus, reduction of heat generated is essential for proper operation of the system. In particular, the 15 stage device introduced within the previous chapter is well suited for solving this thermal issue, as heat can be readily extracted more efficiently as compared to a device with more stages.

When considering an array of ridge lasers, there exists three dominant issues with the configuration:

- The output beam is highly divergent due to a small exit aperture, requiring special facet coatings or external optics
- A large power density through this small exit aperture can lead to catastrophic failure as seen in Figure 5–1.
- In order to minimize mirror losses, it is necessary to cleave the end facet to obtain specular transmission which increase the risk of precious material waste

The solution to these problems exist as a surface emitting LASER. Specifically a ring cavity quantum cascade LASER utilizing 2nd-order distributed-feedback grating to obtain surface emission. However, because emission from opposite sides of the ring is 180 degrees out of phase, destructive interference is observed along the axis of symmetry, resulting in a first order Bessel function intensity profile. [20] [21]Additional azimuthal oscillations in the intensity profile are caused by beating between the grating period and emission wavelength.

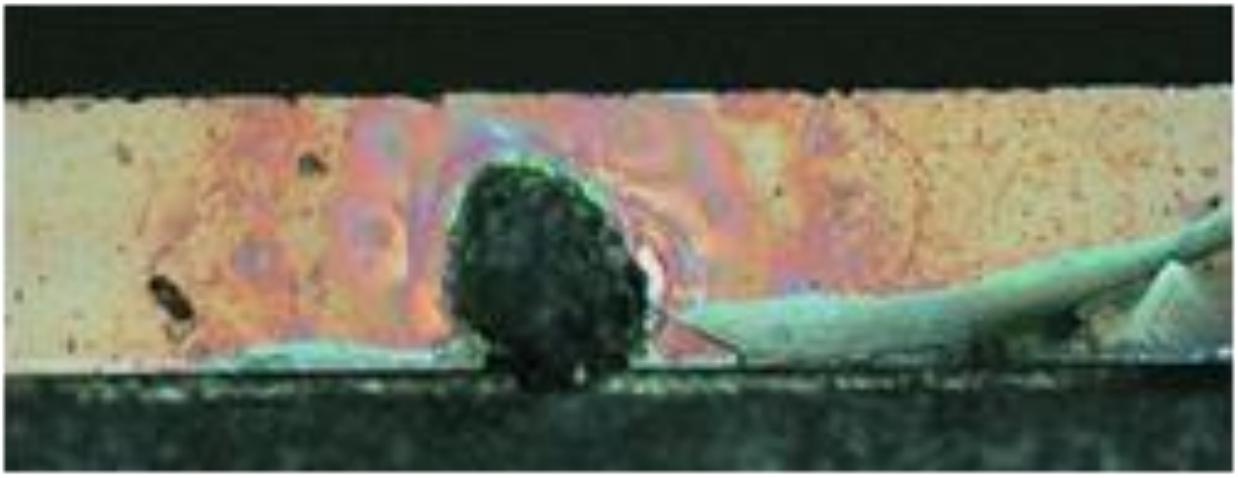

Figure 5–1:Optical microscope image of a QCL destroyed by optical breakdown at the ARC facet.

5.2. Theoretical Considerations

Figure 5–2 presents a schematic of the coordinate system and geometrical parameters. Laser radiation is emitted in the *z* direction from the top facet of the ring. Huygens principle gives for any field component u_p at the observation point P, [22]

$$u_p = \int \frac{kue^{ikR}}{2iR\pi} df_n \tag{5-1}$$

where k is the wavevector magnitude, R is the distance from area element ***df*** to P, and u is the field value at ***df***. The integral is performed over the emitting surface, i.e. the top surface of the ring, and df_n is the projection of the surface area element ***df*** on the direction of the ray from the light source within the ring to df. The area element ***df*** is already in the same direction as the assumed direction vector **n** (z direction) of the rays from the source of emission within the ring to the exit aperture on the top surface of the ring, so that $df_n = df = wad\varphi$, where w is the width of the ring waveguide. Without loss of generality, given the azimuthal symmetry, we may align the coordinates so that the x-axis is directly under the field point P, so that only the polar angle (θ_0) and field point radius vector (R_0) are needed to specify the position of P. The polar angle for the position of each area element is $\theta/2$, so that only the azimuthal angle φ and ring radius a are necessary to specify an area element's position. With these coordinates, the vector from area element to field point P is $\boldsymbol{R} = \boldsymbol{R_0} - \boldsymbol{a} = \{R_o \cdot \sin\theta_o - a \cdot \cos\varphi, -a \cdot \sin\varphi, R_o \cdot \cos\theta_o\}$.

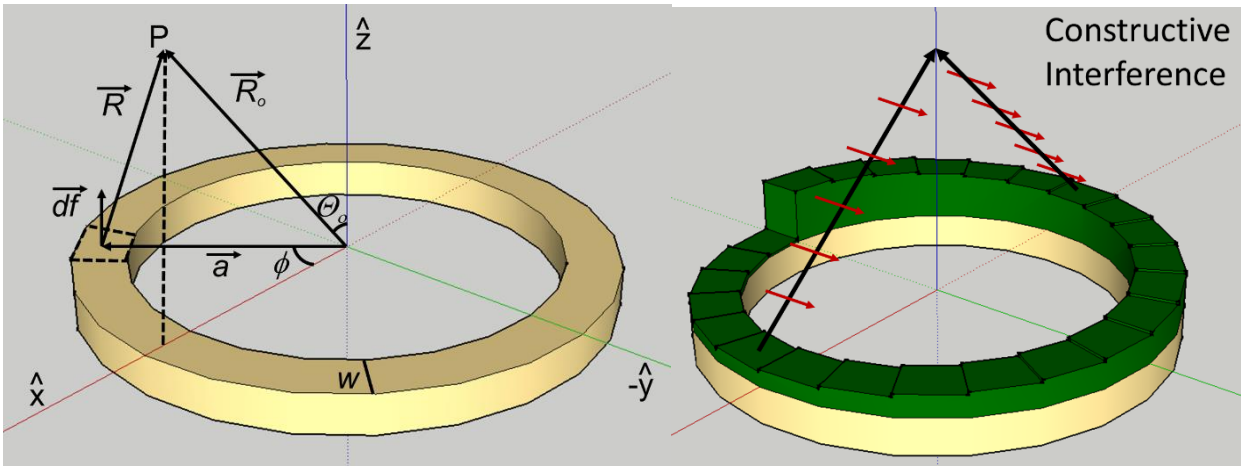

Figure 5–2: (left) Geometry for calculation of ring-cavity emission profile. Field point P lies above the x axis. (right) ring cavity with theoretical spiral phase shifter

Since $a << R_o$, $R = \sqrt{(R_0^2 + a^2 + 2R_0 \cdot a \sin\theta_o \cdot \cos\varphi} \sim R \approx R_0 - a \sin\theta_o \cos\varphi$. Since the range of θ_o is small, keeping the angle dependent terms in the denominator of Eq. (1) gives only slow variations with polar angle, so there we take $R \approx R_0$. On the other hand the factor $k \cdot a$ in the argument of the complex exponential may be large, giving rise to a large phase that oscillates rapidly with small changes in polar angle, so there we must keep the second term in the expansion of R. Then, equation 1 becomes

$$u_p = \frac{wake^{ikR_o}}{2i\pi R_o} \int_0^{2\pi} u e^{-ika \sin\Theta_o \cos\phi} d\phi \tag{5-2}$$

The azimuthally-polarized[10] electric field of the emitted wave at the surface of the ring is $\boldsymbol{E} = E_0\{-\sin\varphi, \cos\varphi, 0\}$. We may then write

$$E_{py} - iE_{px} = \frac{wake^{ikR_o} E_o}{2i\pi R_o} \int_0^{2\pi} e^{-ika \sin\Theta_o \cos\phi} e^{i\phi} d\phi \tag{5-3}$$

E_{Px} calculates to zero because contributions from members of each pair of opposite area elements equally distant from P have opposite sign, and their contributions cancel. However, opposite area elements that have equal but opposite y components are at different distances from P and do not completely cancel. The Bessel function in integral form is

$$J_n(z) = \frac{1}{2i^n \pi} \int_0^{2\pi} e^{iz\cos\phi} e^{in\phi} d\phi \tag{5-4}$$

so that

$$E_{py} = -\frac{wake^{ikR_o} E_o}{R_o} J_1(ka \sin\Theta_o) \tag{5-5}$$

where we have used the property that J_1 is an odd function of its argument.

To eliminate the central node, the anti-symmetry of the ring must be broken. Physically this has been previously demonstrated by means of two $\pi/2$ phase shifts at π phase apart on the ring. In addition we propose a spiraling 3d wedge that may be added to the output facet of the ring. Mathematically, this will alter the phase of the emitted light by a 2π phase shift around the ring and is introduced as an additional angle dependence on the phase term in equation (1). Such a vertical spiral wedge is depicted schematically in Figure 5–2 (right).

$$u_p = \frac{wake^{ikR_o}}{2i\pi R_o}\int_0^{2\pi} ue^{-ika\sin\Theta_o\cos\phi+i\phi}d\phi \tag{5-6}$$

Then

$$E_{py} - iE_{px} = -\frac{wake^{ikR_o}E_o}{iR_o}J_2(ka\sin\Theta_o) \tag{5-7a}$$

$$E_{py} + iE_{px} = \frac{wake^{ikR_o}E_o}{iR_o}J_0(ka\sin\Theta_o) \tag{5-7b}$$

where we have made use of the evenness of the functions J_0 and J_2 with respect to their arguments. Equations (7a) and (7b) give

$$E_{py} = \frac{wake^{ikR_o}E_o}{2iR_o}\left[J_0(ka\sin\Theta_o) - J_2(ka\sin\Theta_o)\right] \tag{5-8a}$$

$$E_{px} = -\frac{wake^{ikR_o}E_o}{2R_o}\left[J_0(ka\sin\Theta_o) + J_2(ka\sin\Theta_o)\right] \tag{5-8b}$$

The intensity obtained by summing the absolute squares of the fields in equations (5) and (8) are plotted as a function of polar angle Θ_0 in Figure 5–3. Results with the wedge show a central peak whereas those without have the usual a central node. [23] [20] [24]

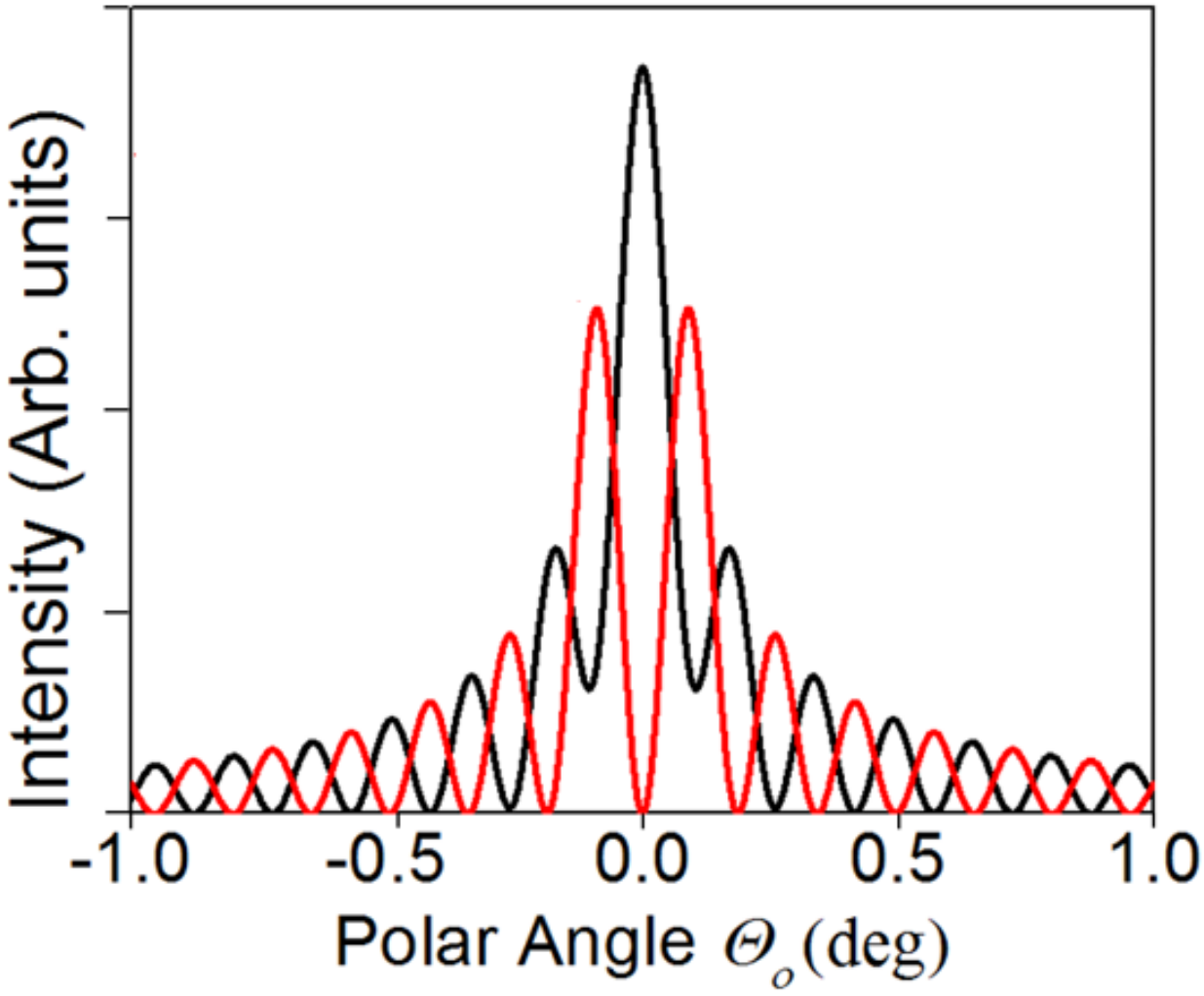

Figure 5–3: Intensity distribution as a function of polar angle Θ_0 with (black) and without the spiral wedge (red).

5.3. Experimental Details

The distributed feedback ring grating is fabricated in a similar manner to the traditional ridge guide with an additional initial lithography step utilized to transfer a circular grating pattern into the cladding layer of the LASER. The surface InP based sample is initially prepared by a bath submersion in buffered oxide etch. Immediately following this, the sample has 750nm of SiO2 deposited on the surface by a PECVD chamber. Following this deposition is 50nm of electron beam evaporated Al2O3 is deposited. Electron beam sensitive PMMA resist is then spun on to the sample to a thickness of ~400nm. A pattern utilizing a LEICA HS 5000+ electron beam writer exposes a radial grating pattern into the resist at a dose of 300μC/cm^2. The pattern is then developed in MIBK:IPA 1:3 for 60s.

Transfer of the electron beam generated pattern to the InP is completed in 3 subsequent etch steps. A BCl3 plasma at 50Watts RIE, 200Watts ICP, 10mTorr, and 20sccm BCL3 was used to selectively remove the Al2O3 over the PMMA with an etch selectivity of ~1:3. Following this plasma, a CF4/O2 plasma was exposed to obtain selectivity of ~15:1 of the SiO2 over the Al2O3 with chamber conditions at 50Watts RIE, 200Watts ICP, 5mTorr, 5sccm O2, 20sccm CF4. To transfer the pattern into the InP substrate, a H2/CH4 plasma was used to obtain a large selectivity of the InP to the SiO2. Chamber conditions were as follows at 200Watts RIE, 600Watts ICP, 5mTorr, 20sccm CH4 and 10sccm of H2. Figure 5–4 shows a patterned device with a DFB grating etched. Figure 5–5 illustrates the steps for this initial patterning stage.

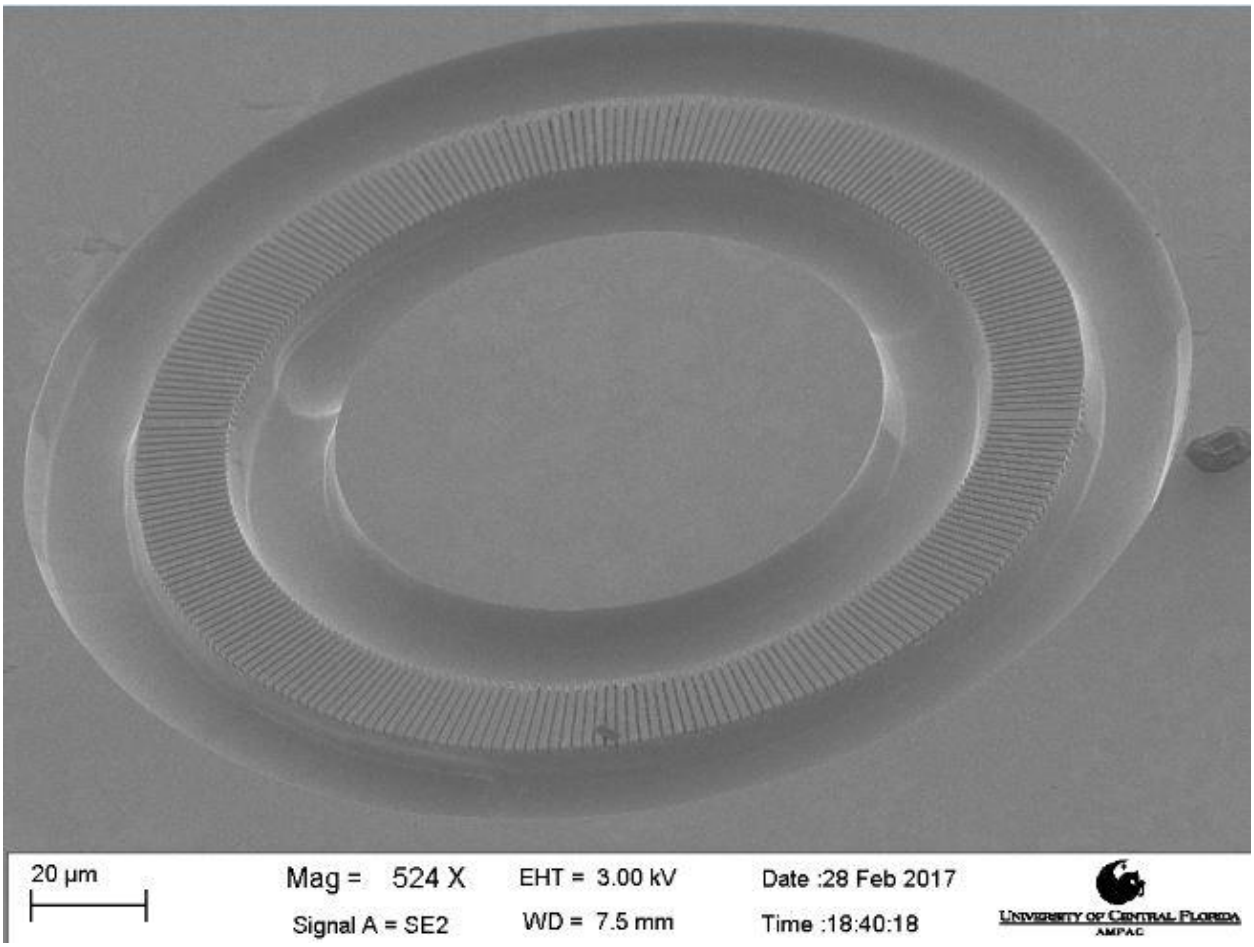

Figure 5–4: Scanning electron microscope image of a DFB pattern etched into the cladding of a ring cavity quantum cascade LASER

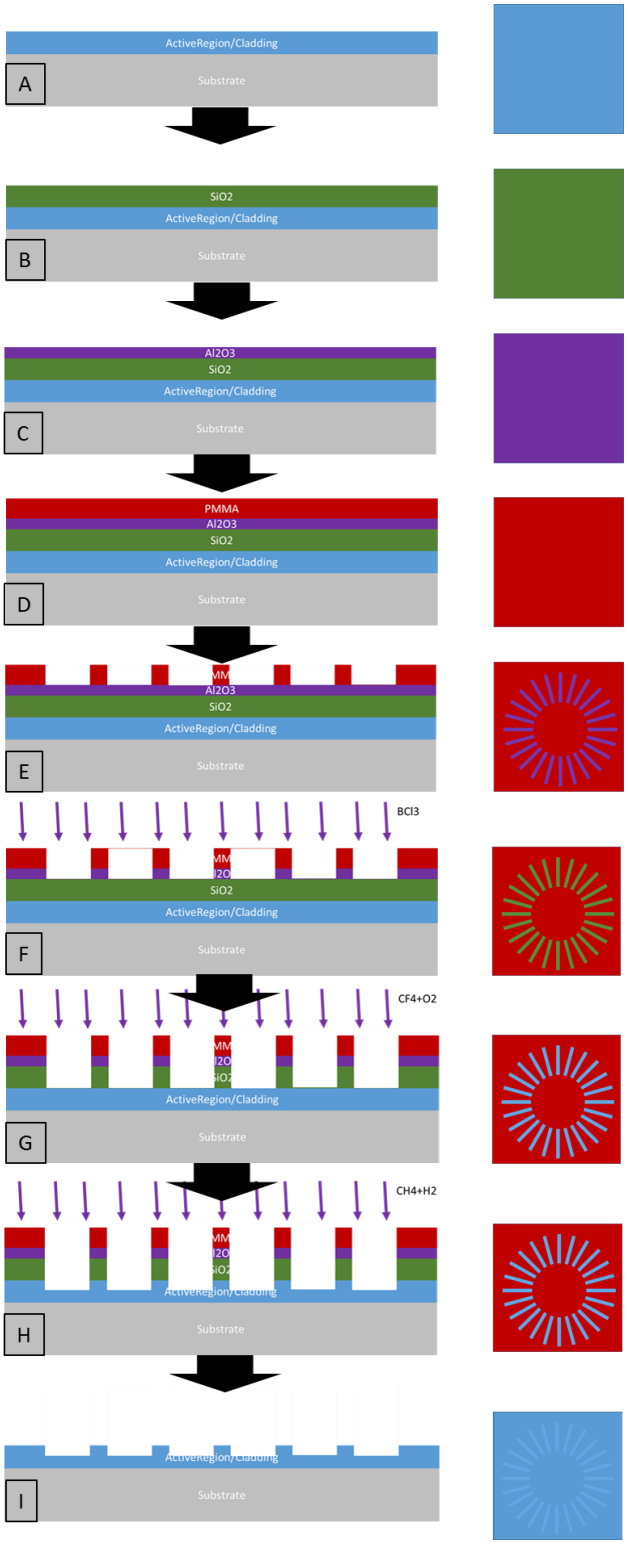

Figure 5–5: Processing steps for distributed feedback grating A) Sample surface is prepared with BOE B) sample is coated with PECVD silica C) Alumina is ebeam deposited D) Electron

beam resist is spun coat and exposed E) Sample is developed in MIBK:IPA 1:3 F) Al2O3 is selectively etched with BCL3 RIE G) SiO2 is selectively etched with CF4 + O2 H) Sample is selectively etched with CH4 +H2 I) BOE is used to remove etch mask

The considered spiral wedge has been fabricated separately utilizing a 3dimensional electron-beam lithography technique. A JEOL scanning electron microscope equipped with Nanometer Pattern Generation System (NPGS) patterned a design in discretized areas using different electron doses. Taking advantage of development rate on dose, the 3-D spiral was fabricated and then transferred into a silicon substrate by an SF6 reactive ion etch plasma. Figure 5–6 presents an optical microscope image of the wedge, and presents the line profile across the wedge. The depth difference between opposite sides is ~350 nm so that the total height of the wedge that has been etched into silicon is d = 700 nm. The phase difference for two waves from opposite sides of the ring with an ideal wedge is λ (n-1) d/λ. We consider the height for a wedge etched into the InP substrate of a substrate-emitting RCSE QCL. For the desired phase difference of π, an index of 3.1 for InP, and a wavelength of 5 μm, the desired wedge height would be 2.4 μm. With optimization of the differential etch rate for mask and wedge material, the desired wedge seems feasible. Additional methodologies of forming the spiral wedge include gray scale mask techniques [25], and direct laser write methods [26].

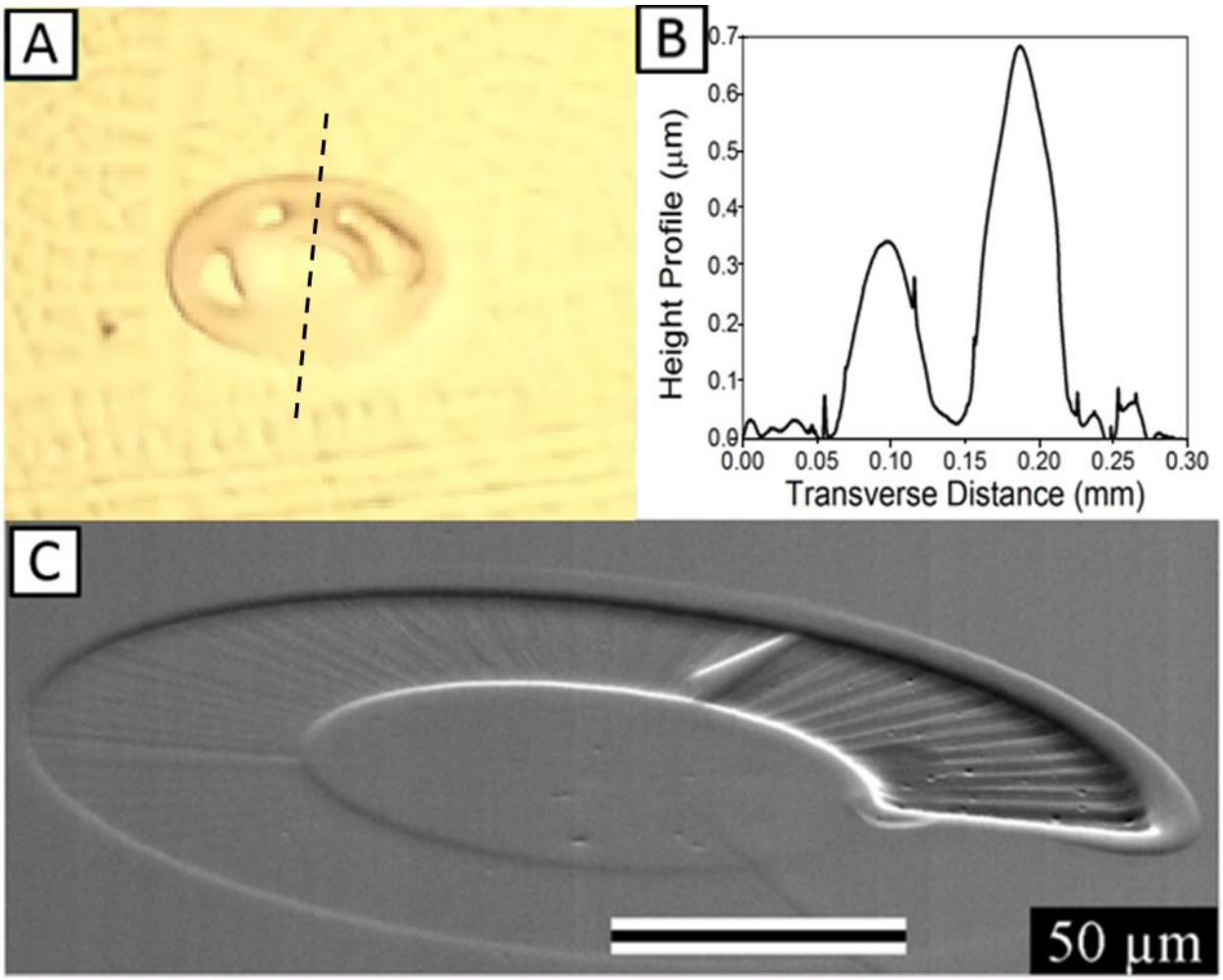

Figure 5–6: (A) Optical image of a 300μm spiral ring fabricated into silicon. The dashed line indicates the profilometer track. (B) Height profile across along the spiral diameter. (C) Angled Scanning Electron Microscope image of the spiral written in e-beam resist

At the time of writing this thesis, this surface emission ring cavity project is still ongoing. The fabrication process of the entire structure including the integration of the distributed feedback grating into the ring waveguide has been established as is shown in Figure 5–4. The project currently is awaiting live material to begin fabricating the ring cavity surface emitting lasers. Once fabricated, devices will be tested, characterized, and implemented into an 2-d arrayed system.

CHAPTER 6: EXTERNAL CAVITY OPERATION UTILIZING AN ACOUSTIC OPTIC MODULATOR

6.1. Introduction

As the dominant high powered, compact, infrared source it comes to no surprise that quantum cascade LASERS are ideally suited for spectroscopic applications. In particular, their high output powers allow for trace and remote sensing of the rotational and vibrational bands of most molecular species. Spectroscopic sensors have numerous applications including but not limited to: combustion sensing [27], trace explosive detection [28], hyperspectral imaging [29], remote sensing [30], industrial gas monitoring [31] and environmental monitoring [32].

For spectroscopic systems in the field, ideal spectroscopic systems require the following properties:

- wavelength tuning over a large range
- narrow linewidths
- Large stable optical output power
- Rapid wavelength tuning
- Compact and rugged

Large optical powers to overcome atmospheric absorption or surface scattering for remote sensing applications, may be obtained by scaling the lateral device dimension. However in doing so, the QCL device is prone to thermal breakdown and reduction of the total number of stages to reduce active region temperature is required as previously discussed.

By inserting a high powered device, such as the one presented here, into an external cavity system utilizing a non-mechanical modulator, one obtains rapid wavelength tuning of single mode output

that is insensitive to vibration, which is ideal for a fielded system. In the following chapter, initial results utilizing the reduced superlattice designed quantum cascade laser with an electrically controlled acousto-optic modulator is presented.

6.2. The Experimental Setup

The external cavity system implementing an acousto-optic modulator is shown in Figure 6–1. A radio frequency signal is applied to a piezoelectric transducer which creates a travelling acoustic wave in a germanium crystal. The created sound wave produces a spatial periodic variation in the germanium's refractive index due to compressions and rarefactions of the sound wave. This periodic refractive index modulation creates a diffraction effect when an incident optical beam enters the crystal. That is, when an optical beam is incident on the acousto optic modulator, a wavelength dependent deflection occurs, according to

$$\theta = \sin^{-1}(\frac{m \cdot \lambda}{\Lambda})$$

If a mirror is placed at the center frequency of the deflected beam, a narrow band of wavelengths proportional to the optical path length of the diffracted beam reflects back into the quantum cascade laser creating a Fabret perot cavity. Due to mode competition, these selected wavelengths increase in gain each pass and are output at the opposite facet. Optical power emitted from each facet of the laser was collimated with an antireflection coated ZnSe lens. The mirror in the external cavity was placed 9cm from the output of the acousto-optic modulator and aligned to the first order diffracted beam.

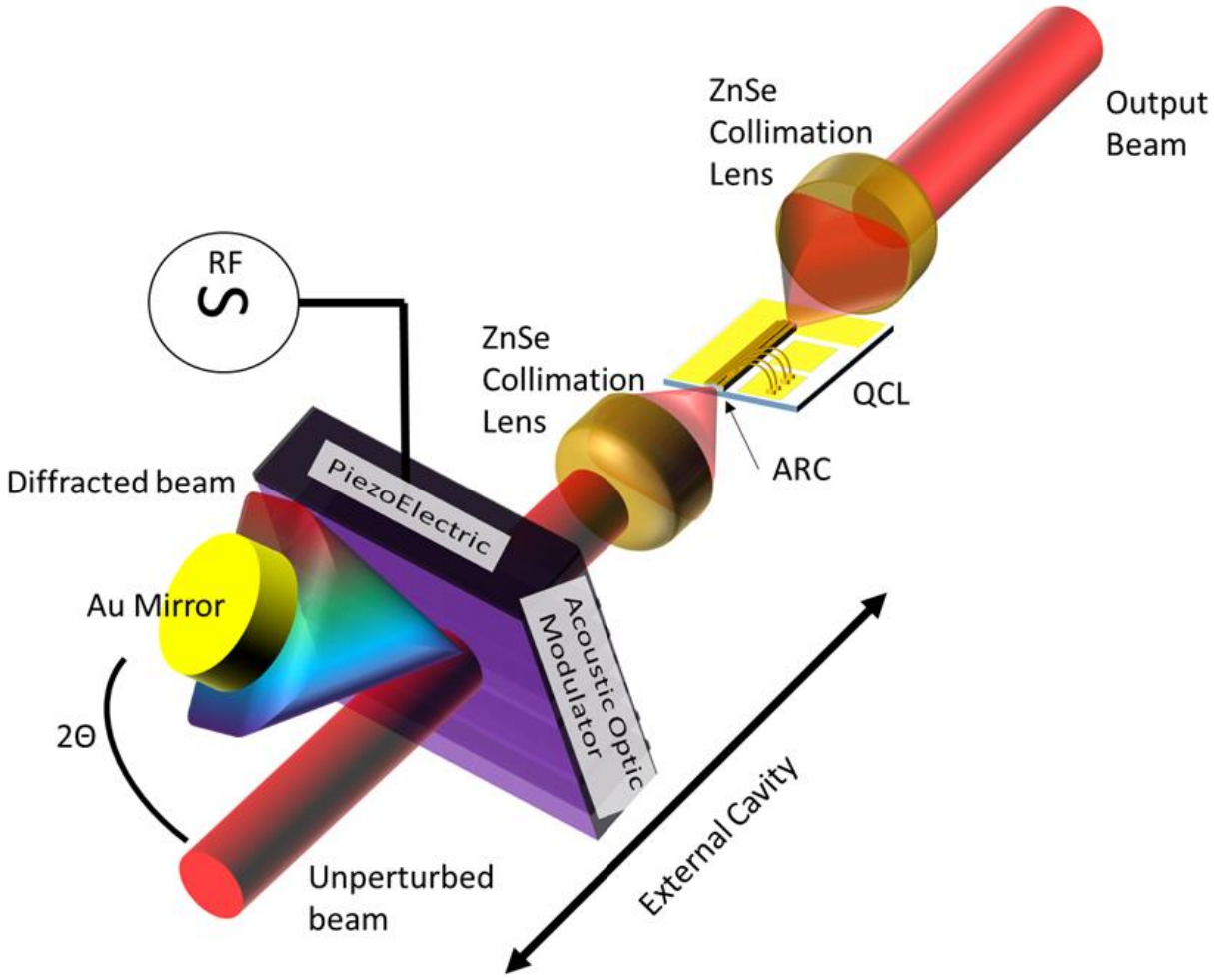

Figure 6–1: Diagram of a quantum cascade laser in an external cavity utilizing and acousto-optic modulator

The quantum cascade LASER utilized is a ridge-waveguide type where the lasing region is confined laterally to 10.4µm at a depth of 6.5µm below the surface and extends ~3.1mm in length. The QCL was mounted epitaxial side down such that the lasing region was closer to the sub-mount for heat removal, as shown in Figure 6–2.

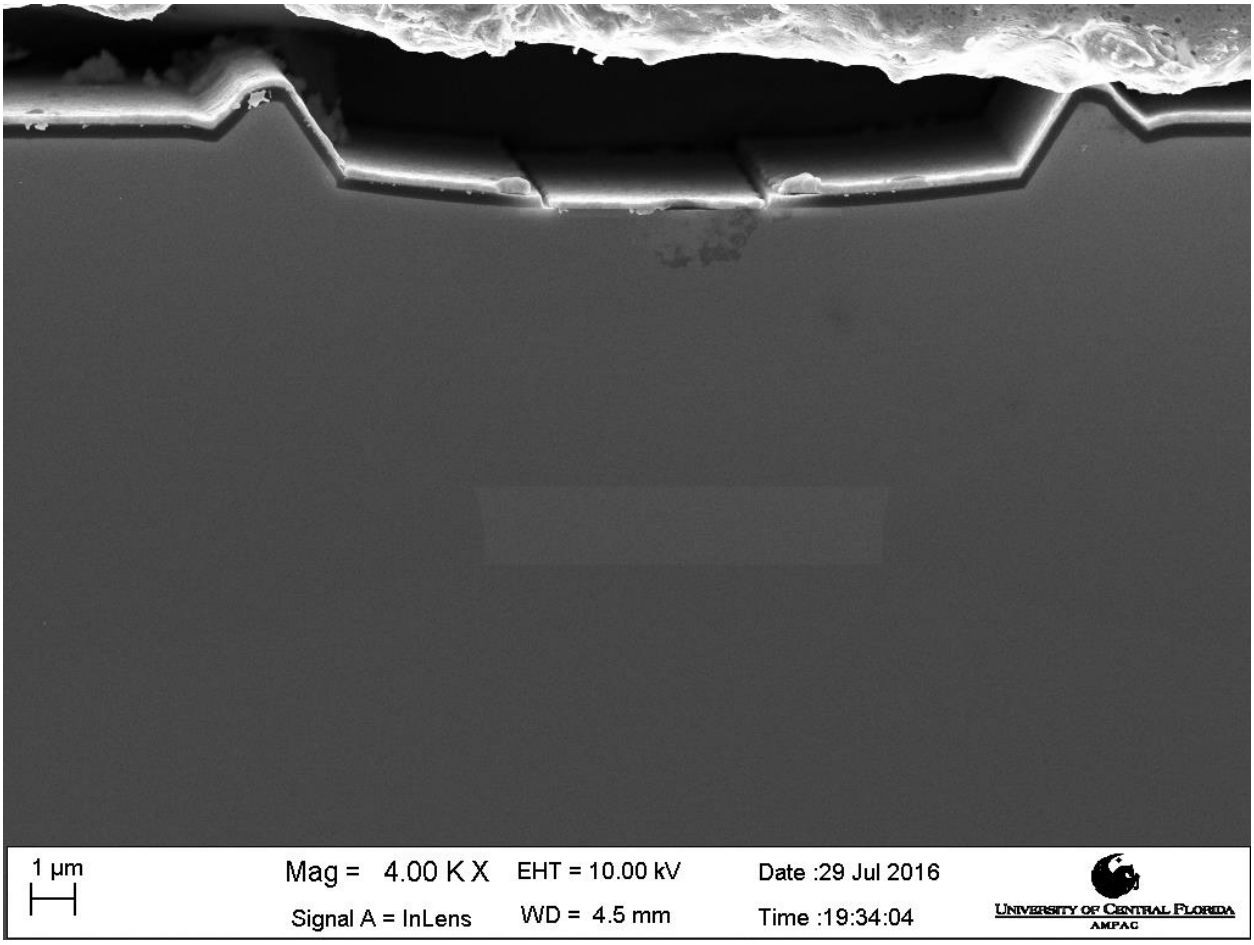

Figure 6–2: Scanning Electron Microscope image of the QCL ridge lasing channel below sub-mount. The area above the channel is sub-mount AuSn solder

In order for the quantum cascade laser to operate with wavelength selection dictated in an external cavity, it became necessary to remove the on chip Fabret Perot cavity between the two LASER facets. This was done by applying a thin antireflection coating on one facet, by means of an electron beam physical vapor deposition chamber. Figure 6–3 presents the optical output power curves of the device before and after the anti-reflection coating was deposited. The data presented was collected in pulsed operation at 10kHz with a pulse width of 600ns.

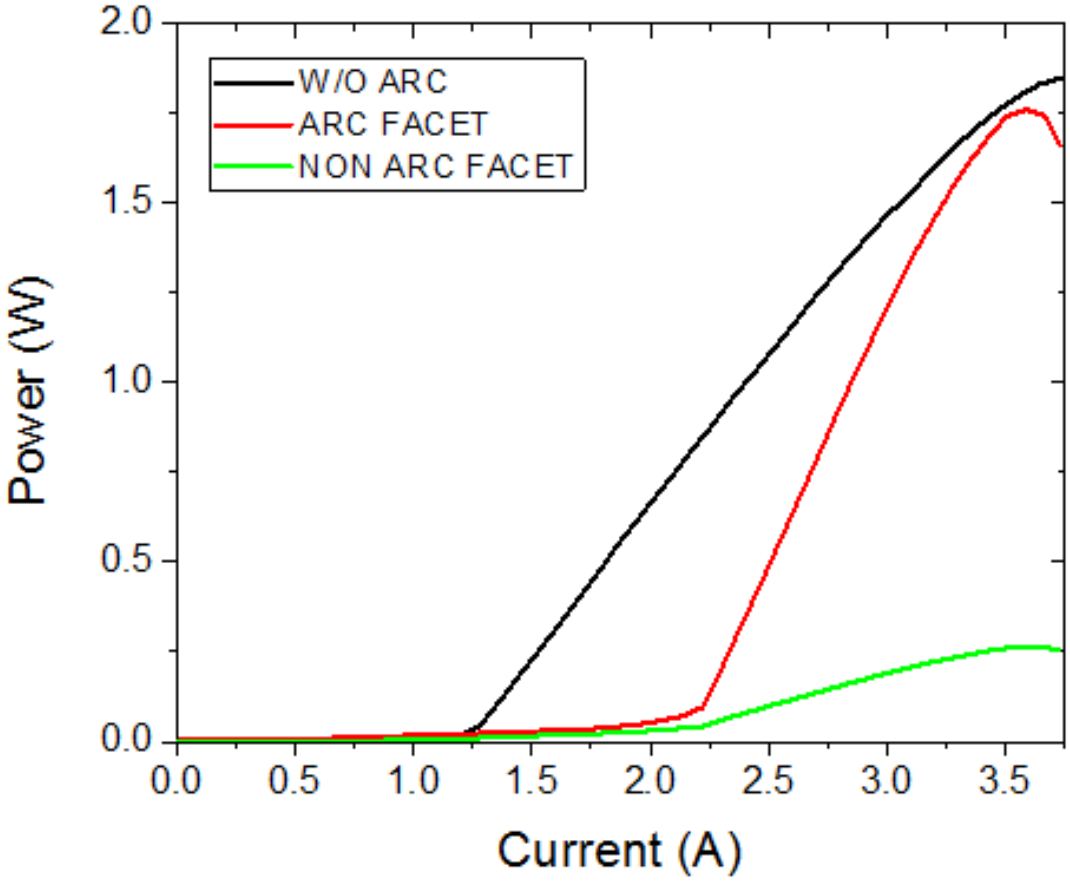

Figure 6–3: Light-Current Curve for the Quantum Cascade LASER without an anti-reflection Coating (black) and with an anti-reflection coating out of each facet (green & red).

The radio frequency driver of the acousto-optic modulator ranged from 30MHz to 60MHz. The QCL was operated in pulsed-mode operation at 1.25A with a pulse width of 125ns and duty cycle of 5%. The power applied to the acoustic-opto modulator was ~11.25W. Figure 6–4 displays the spectral output of an AOM in external cavity while varying RF input frequency. The emission wavelength for the external cavity system spanned ~200cm^{-1} ranging from 1725cm^{-1} to 1925cm^{-1}. The measured QCL emission spectrum linewidth for the central gain frequency of ~1825cm^{-1} was ~8cm^{-1}.

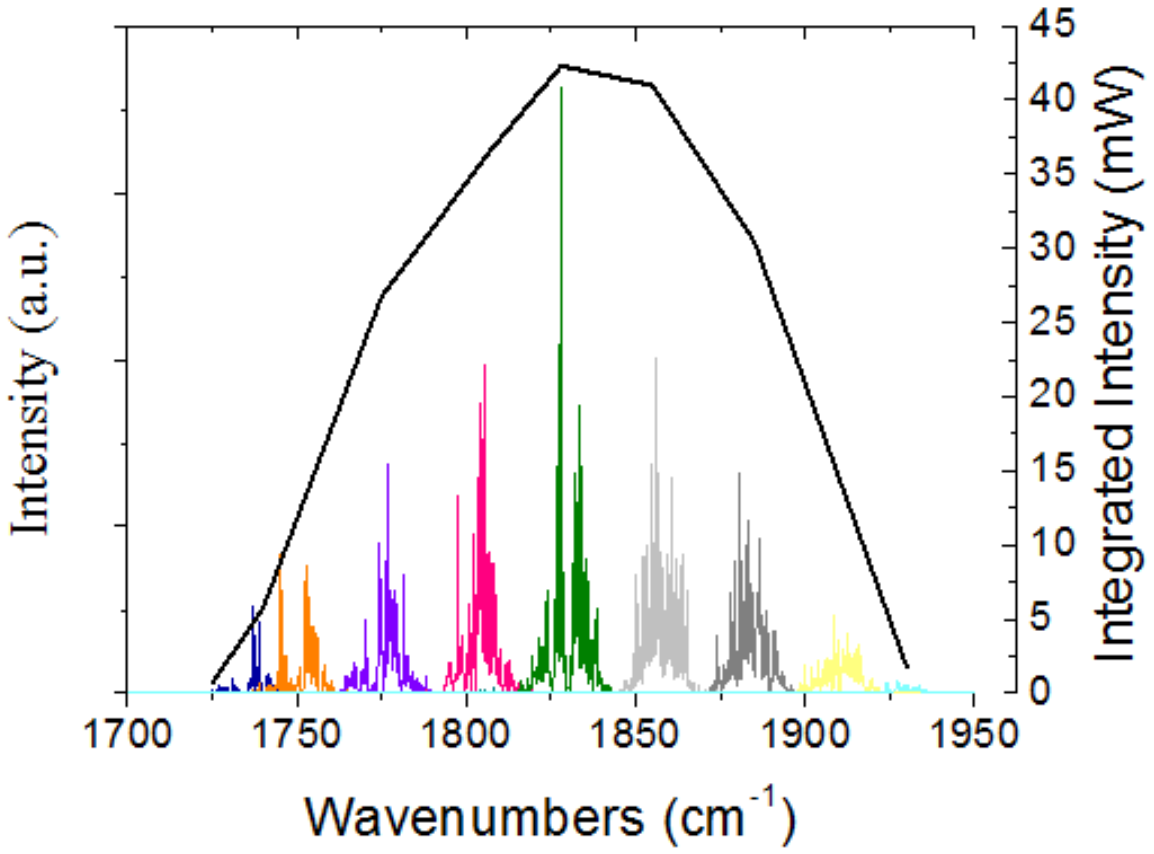

Figure 6–4: Spectral emission span of the cavity achieved by tuning the AOM with input RF frequency while operating in pulsed mode. The thick black line corresponds the measured intensity of the beam, whereas each color represents an emission spectra obtained by a different RF frequency into the AOM. The center frequency corresponding to an input frequency of 40.8MHz and the two outer limits at 38.07MHz and 43.3MHz. The approximate spectral width of each tuned emission spectra is 8cm^{-1}.

If the QCL is instead driven at the pulse driver's maximum pulse width (1µs) and maximum duty cycle (5%), the average spectral width drops to ~4.5cm^{-1} at the cost of the total spectral range for a driving current of 1.25A decreasing the spectral span from 200cm^{-1} to nearly 100cm^{-1}. This is evident in Figure 6–5.

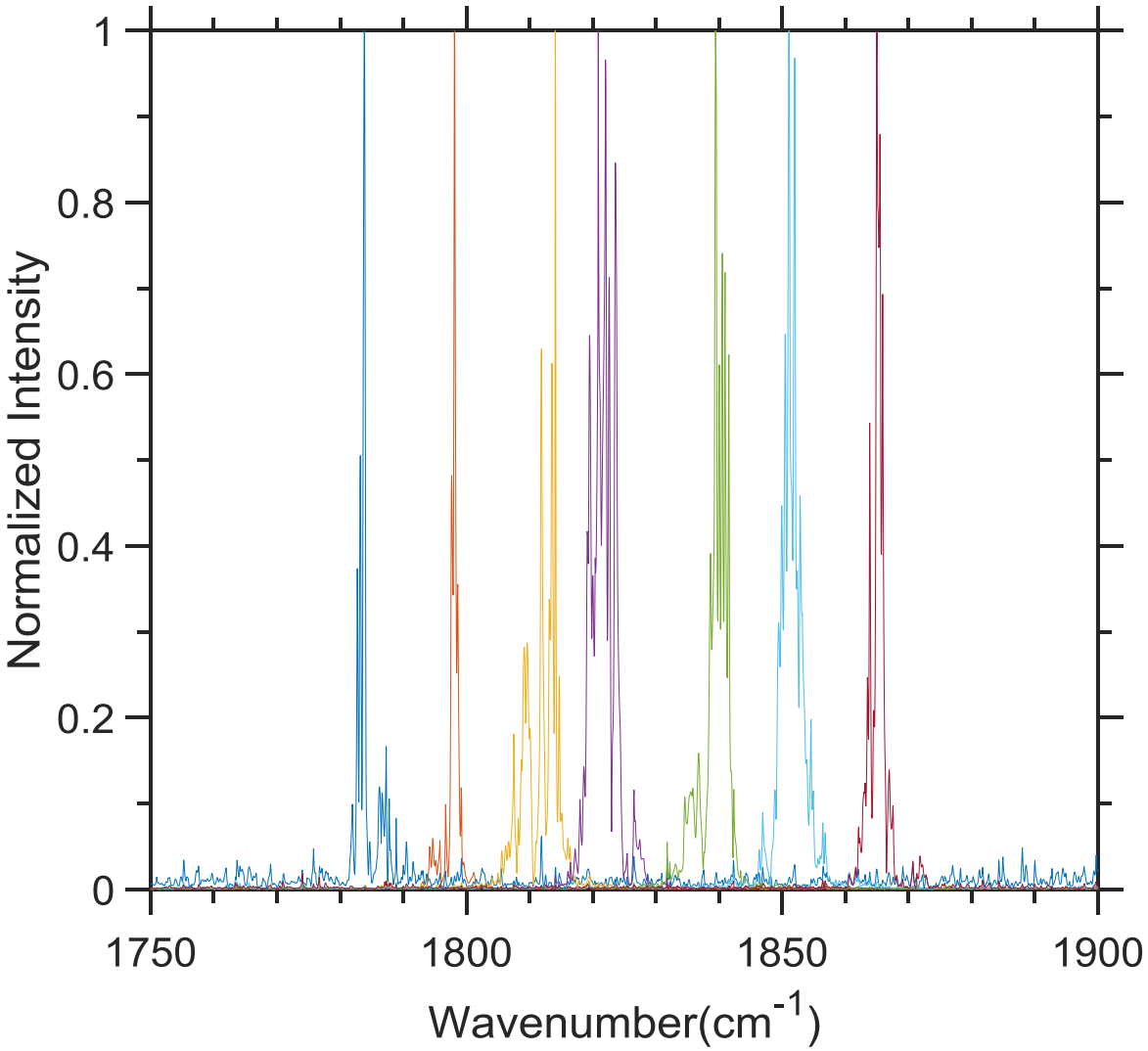

Figure 6–5:Spectral emission span of the cavity achieved by tuning the AOM with input RF frequency while operating in pulsed mode at 5% duty cycle and 1µs pulse width. Each color represents an emission spectra obtained by a different RF frequency into the AOM. The center frequency corresponding to an input frequency of 40.8MHz and the two outer limits are at 39.08MHz and 41.1MHz. The approximate spectral width of each tuned emission spectra is 4.5cm^{-1}.

We can further decrease the spectral linewidth of emission by allowing the QCL to operate in continuous wave as shown in Figure 6–6. The approximate spectral width of the emission spectra is ~3cm^{-1}. The AOM for continuous wave was kept at a frequency of 41MHz.

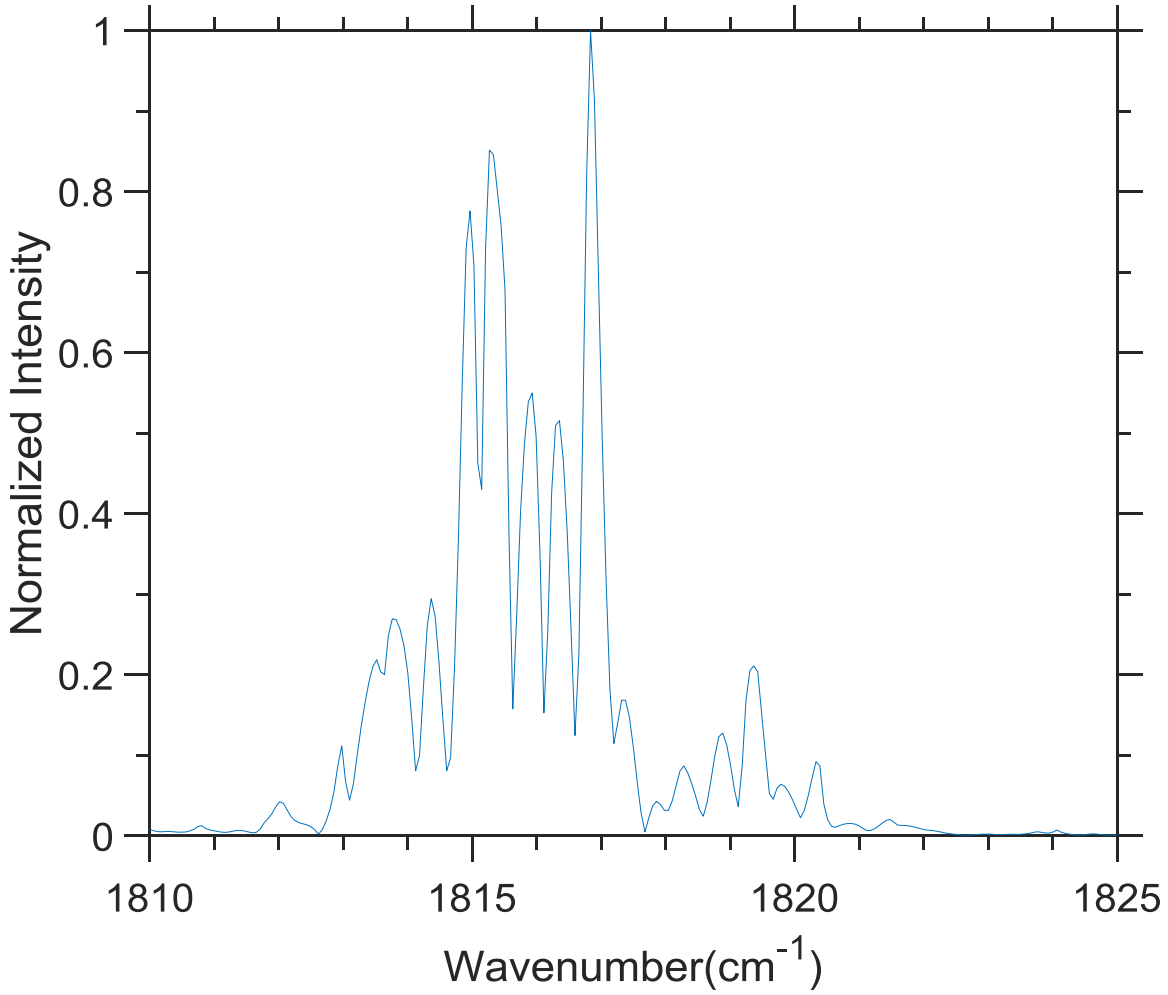

Figure 6–6: Spectral emission of the cavity operated in continuous wave with fixed AOM frequency ~41MHz. The approximate spectral width is ~3cm^{-1}.

Demonstration of the rapid spectral tunability of the quantum cascade LASER in an acousto-optic modulator external cavity, is presented in Figure 6–7. Acetone vapor was measured utilizing an infrared photovoltaic detector sold by Boston Electrons, with a response time <1ns. Multiple scans were taken with the AOM's frequency modulated by a saw tooth wave at a frequency of 140kHz, from 38MHz to 43MHz, covering the full range presented in Figure 6–5. The QCL was operated in this pulsed regime in order to have the largest spectral span to observe desired spectral features at wavenumbers below 1800cm^{-1}. Two sample scans were taken; one of the emission of the QCL

AOM external cavity, another with acetone vapor and the last with a Formaldehyde gas cell placed in front of the detector. The high vapor pressure of acetone and strong absorption band at ~1750cm^{-1} cut off the left portion of the spectra corresponding to the lower wavenumbers.

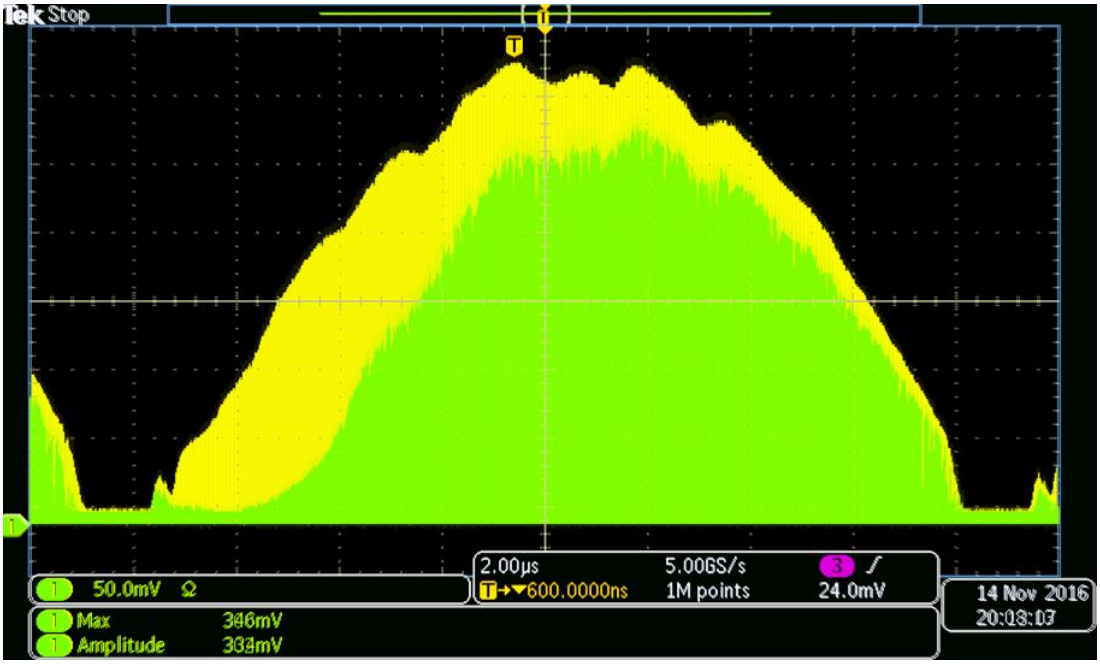

Figure 6–7: Oscilloscope output of infrared photovoltaic detector signal measured over multiple scans of the QCL emission output (yellow) and that of acetone vapor (green-above) placed in line of the detector

This system was built under a contract for a phase I grant granted by the Air Force. Its intent was to be used for a novel application of real time measurements for combustion diagnostics. Currently results are being reviewed by the Air Force and cannot be published during the time of writing this thesis.

CHAPTER 7: CONCLUDING REMARKS

Focus of this work is on the reduction of the number of stages within the superlattice of a quantum cascade laser to reduce cost of the device and allow for power scaling. A quantum cascade laser with a reduced number of stages is investigated and characterized in terms of device performance. Additionally it was also shown how this novel design may be advantageous for particular system level applications.

A structure referenced in [10] was grown only with nearly a third of the number of active region stages. This device was then processed following standard semiconductor techniques into a buried heterostructure ridge emitting device of 10μm width by 2.1μm length. Optical power and voltage measured against injection current was measured in pulsed and continuous wave operation at room temperature. These measured characteristics were compared against the structures measured in [10] and [15]. By reducing the number of stages it was shown that the current threshold was not substantially increased as the threshold current is mostly dominated by the transparency current term. It was also shown that due to the reduced slope efficiency of the device, the maximum current allowed was increased by design of the sheet density and coupling factor in order to allow for larger optical output powers.

As compared to the sister sample in [10] with 40 stages, the 15 stage device performance presented here is comparable. A reduction of wall plug efficiency from 28% to ~20% was observed between the two samples. Slope efficiency per stage between the two devices were identical.

Thermal simulations of the active region and device were also investigated utilizing a commercial simulation package (COMSOL). Investigations from thermal transport simulation reveal that because of the low thermal conductivity of the ternary materials utilized within the active region,

reduction of the number of stages resulted in a lower active region temperature when operating in high duty cycle operation. Specifically it was shown that whilst maintaining the same injection current density, that for a reduced 15 stage device the lateral dimension of the superlattice could be nearly ~6x larger before the maximum temperature of the active region is equal to that of a 40 stage device. This is particularly promising for further developing the technology in the pursuit of larger output powers from a single quantum cascade laser.

When operating the device from pulsed operation to continuous wave operation, the change in the following figure of merits were small indicating that the active region was not significantly overheating causing severe degradation of device performance. The slope efficiency had a reduction of 2% and the threshold current density had a minor 16% increase. Optical power densities in pulsed operation were observed to be 1.07W/mm and in continuous wave operation observed to be larger than 0.5W/mm which is larger than the device produced in [15], leading to the possibility of larger optical power outputs by the increase of cavity length and later width of the device.

Further, it was shown that the device could be processed into a ring cavity surface emitting device as opposed to a traditional edge emitting laser. The ring cavity configuration, although processing complexity has increased, has the added benefits of lower risk of catastrophic optical damage due to the high power densities confined within a small region, less divergence from a larger exit aperture and ease of die formation as compared to its ridge counterpart. Particular applications that are in particular well suited for this design are infrared scene projection and hyperspectral imaging, where a 2-d spatially arrayed quantum cascade lasers are needed for the system. Although no surface emission was observed during the duration of this project, phase II is actively being

pursued and additional funding resources to continue the DFB incorporation for surface emission is being investigated.

Additionally it was demonstrated that this particular QCL with its high output power in the continuous wave regime is well suited for applications where a signal may exist in a broad attenuating background. Applications which benefit include short range remote sensing through non-atmospheric windows or gas combustion diagnostics systems. Both of which rely on absorption spectroscopy to determine species identification. By destroying the Fabret Perrot cavity intrinsic to the laser and creating an external cavity with mirror and phase grating, single longitudinal mode output could be obtained. Through modulation of the phase grating (acoustic optic modulator) the wavelength dominant within the cavity would fire external to the cavity by simple mode domination of stimulated emission. This system was built under a contract for a phase I grant granted by the Air Force. Its intent was to be used for a novel application of real time measurements for combustion diagnostics. Currently results are being reviewed and cannot be published during the time of writing this thesis.

APPENDIX A: THE MULTI-WELL PROBLEM

The single well potential also known as the particle in a box is a well-known introductory quantum mechanical problem studied to illustrate quantum effects. The problem is well known and further information on solving the single well analytically is established in many published text books. [33] [34] [35] For the purpose of this thesis we suppose there exists a multi-well problem and approach the solution numerically.

We begin with the time independent Schrodinger equation.

$$\frac{p^2}{2m^*}\Psi + U\Psi = E\Psi \tag{A-1}$$

In the expansion of equation A-1, we must in general allow for the effective mass m* to vary with growth direction as dissimilar semiconductor epitaxial layers may have dissimilar effective masses. Equation A-1 may be written as

$$\delta_z \frac{\hbar^2}{2m^*}\delta_z\Psi + U\Psi = E\Psi \tag{A-2}$$

Expansion of the first partial spatial derivative as a finite difference approximation of equation A-2 leads to

$$\frac{\frac{\hbar^2}{2m^*(z+\delta_z)}\cdot\delta_z\Psi|_{z+\delta_z} - \frac{\hbar^2}{2m^*(z-\delta_z)}\cdot\delta_z\Psi|_{z-\delta_z}}{2\delta_z} + U\Psi(z) = E\Psi(z) \tag{A-3}$$

Continuing the expansion with centered defined expansion of A-3

$$\frac{\frac{\hbar^2}{2m^*(z+\delta_z)}\cdot\frac{\Psi(z+2\delta_z)-\Psi(z)}{2\delta_z} - \frac{\hbar^2}{2m^*(z-\delta_z)}\cdot\frac{\Psi(z)-\Psi(z-2\delta_z)}{2\delta_z}}{2\delta_z} + U\Psi(z) = E\Psi(z) \tag{A-4}$$

$$\frac{\Psi(z+2\delta_z)-\Psi(z)}{m^*(z+\delta_z)} - \frac{\Psi(z)-\Psi(z-2\delta_z)}{m^*(z-\delta_z)} = \frac{8\cdot{\delta_z}^2}{\hbar^2}(E-U)\Psi(z) \tag{A-4}$$

$$\frac{\Psi(z+\delta_z)}{m^*\left(z+\frac{\delta_z}{2}\right)} =\cdot \left([\frac{2\cdot{\delta_z}^2}{\hbar^2}\cdot(E-U) + \frac{1}{m^*\left(z-\frac{\delta_z}{2}\right)} + \frac{1}{m^*\left(z+\frac{\delta_z}{2}\right)}]\cdot\Psi(z) - \frac{\Psi(z-\delta_z)}{m^*\left(z-\frac{\delta_z}{2}\right)}\right) \tag{A-5}$$

Where we have transformed 2δz to δz. The effective mass may be found at its neighboring points. [26]

$$m^*\left(z \pm \frac{\delta_z}{2}\right) = \frac{m^*(z \pm \delta_z) + m^*(z)}{2} \tag{A-6}$$

Consideration of non-degenerate solutions allows for uniqueness of the eigenvalue problem and allows for the numerical calculation of equation A-5 by means of a shooting method. Methodology of the shooting method begins by initializing the boundary conditions of $\psi(0)=0$ and $\psi(\delta z)=1$, iterating through eigenenergies and solving equation A-5 for the entire wave function. We converge on solutions of the defined potential due to the existence of only a discrete set of eigenenergies that are solutions to the time independent Schrodinger equation; all other values cause divergence of when solving for the wave function. Figure A1 illustrates the methodology of the numerical method.

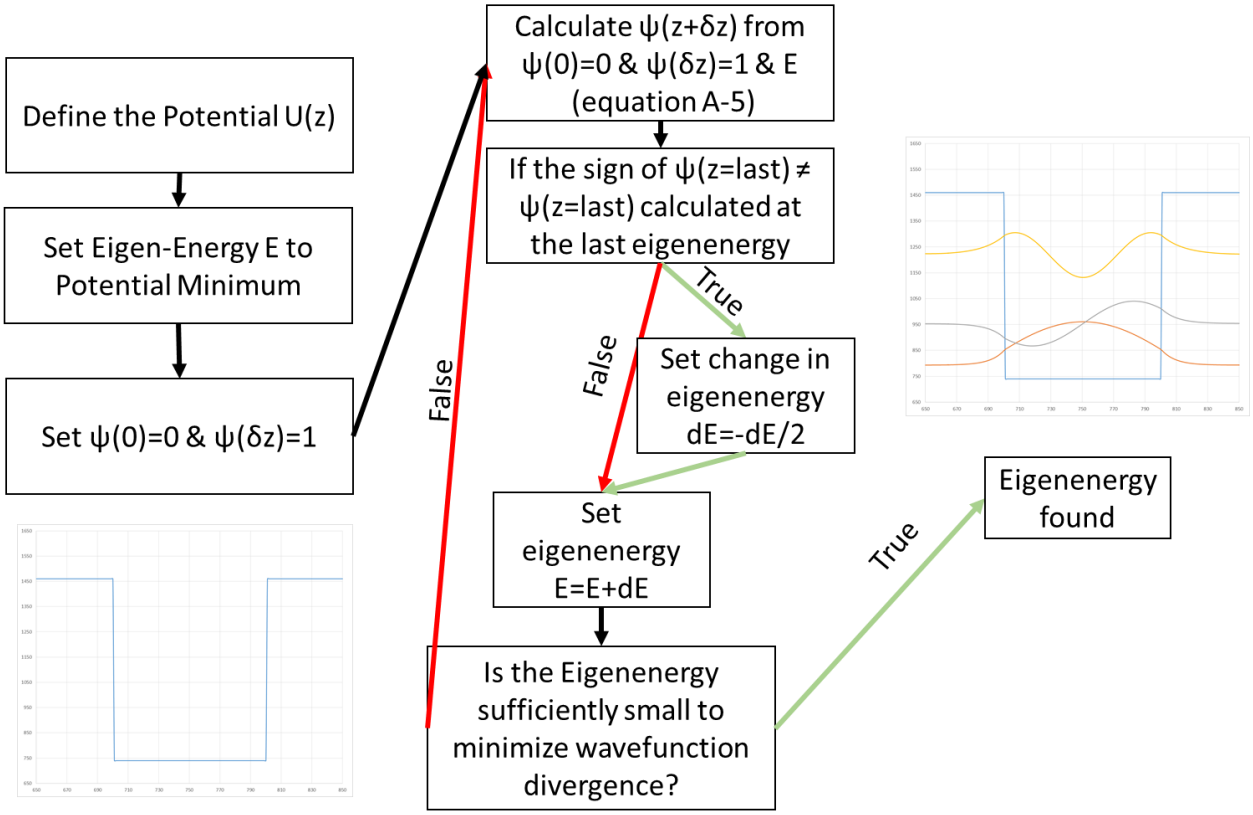

Figure A-1: Diagram illustrating methodology of shooting method of multi-well problem with finite energy.

The numerical shooting method is a powerful tool essential towards the design of quantum cascade LASERS.

APPENDIX B: LIST OF PUBLICATIONS

Journal Publications

1. P.N. Figueiredo, I.O. Oladeji, A.P. Warren, E.M. Smith, J.W. Cleary, R.E. Peale, "Carbon-black film by spray and spin deposition" (in preparation)
2. P.N. Figueiredo, A. Dillard, N. Concors, E. Smith, A Warren, R John, P.S. Davids, P.S. Finnegan, D.B. Burckel, J. Ginn, R.E. Peale, "Directional Emission from a 2-Dimensional Cuboid Array" (in preparation)
3. P. Figueiredo, M. Suttinger, R. Go, A. Todi, H. Hsu, E. Tsvid, C. Kumar N. Patel, A. Lyakh "Narrow Ridge Buried Heterostructure Continuous Wave Quantum Cascade Lasers with Reduced Number of Stages" Photonics Technical Letters (submitted)
4. A Lyakh, M Suttinger, R Go, P Figueiredo, A Todi, "5.6 μ m quantum cascade lasers based on a two-material active region composition with a room temperature wall-plug efficiency exceeding 28%" Applied Physics Letters 109 (12), 121109 (2016)
5. E.M. Smith, D. Panjwani, J. Ginn, A.P. Warren, C. Long, P. Figuieredo, C. Smith, J. Nath, J. Perlstein, N. Walter, C. Hirschmugl, R. E. Peale, D. Shelton, "Dual band sensitivity enhancements of a VOx microbolometer array using a patterned gold black absorber," Applied Optics 55 (8), 2071-2078 (2016)
6. D.B. Burckel, P.S. Davids, P.S. Finnegan, P.N. Figueiredo, J.C. Ginn, "Directional emissivity from two-dimensional infrared waveguide arrays," APL 107 (12), 12902 (2015)
7. I Rezadad, J Boroumand, E Smith, P Figueiredo, Robert E. Peale "Stress Analysis of Free-Standing Silicon Oxide Films Using Optical Interference" MRS 1536, pp. 155-160 (2013)

8. F K. Rezaie, C J. Fredericksen, W R. BuchwalD, J W. Cleary, E M. Smith, I Rezadad, J Nath, P Figueiredo, M Shahzad, J Boroumand, M Yesiltas, G Medhi, A Davis, R E. Peale "Planar integrated plasmonic mid-IR spectrometer" MRS 1510 (2013)
9. T. Brusentsova, R. E. Peale, D. Maukonen, P. Figueiredo, G. E. Harlow, D. S. Ebel, A. Nissinboim, K. Sherman, and C. M. Lisse, "Laboratory far-infrared spectroscopy of terrestrial sulfides to support analysis of cosmic dust spectra," Mon. Not. R. Astron. Soc. 420, 2569–2579 (2012).

Conference Proceedings

1. P.N. Figueiredo, A Muraviev, RE Peale "Ring cavity surface emitting quantum cascade laser with a near Gaussian beam profile" SPIE Defense/Security May 2015
2. P. Figueiredo, J. Nath, G. Medhi, A. Muraviev, C. J. Fredricksen, W. R. Buchwald, J. W. Cleary, R. E. Peale, "Planar integrated plasmonic mid-IR spectrometer," Proc. SPIE 8155A - 2 (2011), Invited.
3. P. Figueiredo, M. Suttinger, R. Go, A. Todi, H. Hsu, A. Lyakh, E. Tsvid, C. Kumar N. Patel, "High Performance 40-stage and 15-stage Quantum Cascade Lasers Based on Two-Material Active Region Composition" SPIE Defense/Security April 2017
4. E Smith, J Boroumand, I Rezadad, P Figueiredo, J Nath, D Panjwani, R. E. Peale, O Edwards, "MEMS clocking-cantilever thermal detector" SPIE Defense/Security April 2013
5. J Nath, D Maukonen, E Smith, P Figueiredo, G Zummo, D Panjwani, R E. Peale, G Boreman, J W. Cleary, K Eyink, "Thin-film, wide-angle, design-tunable, selective absorber from near UV to far infrared" Proc. SPIE 8704 - 127 (2013)

6. C J. Fredricksen, JW. Cleary, W R. Buchwald, P Figueiredo, F Khalilzadeh-Rezaie, G Medhi, I Rezadad, M Shahzad, M Yesiltas, J Nath, J Boroumand, E Smith, R E. Peale "Planar integrated plasmonic mid-IR spectrometer" SPIE Infrared Tech & Appl. 2012

REFERENCES

[1] W. Herschel, "Experiments on the Refrangibility of the Invisible Rays of the Sun," *Philosophical Transactions of the Royal Society*, pp. 284-292, 1800.

[2] A. Siegman, LASERS, University Science books, 1986.

[3] J. Faist, F. Capasso, D. L. Sivco, C. Sirtori, A. L. Hutchinson and Cho A. Y., "Quantum Cascade Laser," *Science*, vol. 264, pp. 553-556, 1994.

[4] B. Lax, "Cyclotron resonance and impurity levels in semiconductors," in *Proceedngs of the International Symposium on Quantum Electronics*, 1960.

[5] R. N. Hall, G. E. Fenner, J. D. Kingsley, T. J. Soltys and R. O. Carlson, "Coherent Light Emission From GaAs Junctions," *Physical Review Letters*, vol. 9, no. 9, pp. 366-368, 1962.

[6] R. Kazarinov and R. Suris, "Possibility of amplification of the electromagnetic waves in a semiconductor with a superlattice," *Soviet Pysics Semiconductor*, vol. 5, pp. 707-709, 1971.

[7] M. B. Panish, I. Hayashi and S. S., "DOUBLE-HETEROSTRUCTURE INJECTION LASERS WITH ROOM-TEMPERATURE THRESHOLDS AS LOW AS 2300 A/cm2," *Applied Physics Letters*, vol. 16, p. 326, 1970.

[8] Z. I. Alferov, V. M. Andreev, D. Z. Garbuzov, Y. V. Zhilyaev, E. P. Morozov, E. L. Portnoi and V. G. Trofim, "Investigation of the influence of the AlAs-GaAs heterostructure parameters on the laser threshold current and realization of continuous emission at room temperature," *Soviet Physics Semiconductor*, vol. 4, p. 1573, 1971.

[9] R. Paiella, "Quantum Cascade Lasers: Overview of Basic Principles of Operation and State of the Art," in *Intersubband Transitions in Quantum Structures*, New York, McGraw-Hill, 2006, pp. 1-44.

[10] A. Lyakh, M. Suttinger, R. Go, P. Figueiredo and A. Todi, "5.6 μ m quantum cascade lasers based on a two-material active region composition with a room temperature wall-plug efficiency exceeding 28%," *Applied Physics Letters,* vol. 109, p. 121109, 2016.

[11] A. Hugi, R. Terazzi, B. Yargo, A. Wittmann, M. Fischer, M. Beck, J. Faist and E. Gini, "External cavity quantum cascade laser tunable from 7.6 to 11.4μm," *Applied Physics Letters,* vol. 95, p. 061103, 2009.

[12] J. Faist, Quantum Cascade Laser, Oxford: Oxford University Press, 2013.

[13] L. Diehl, D. Bour, S. Corzine, J. Zhu, G. Höfler, M. Lončar, M. Troccoli and F. Capasso, "High-power quantum cascade lasers grown by low-pressure metal organic vapor-phase epitaxy operating in continuous wave above 400K," *Applied Physics Letters,* vol. 88, p. 201115, 2006.

[14] Y. Hu, L. Wang, J. Zhang, L. Li, J. Liu, F. Liu and Z. Wang, "Facet temperature distribution of a room temperature continuous-wave operating quantum cascade laser," *Journal of Physics D: Applied Physics,* vol. 45, no. 32, p. 325103, 2012.

[15] A. Lyakh, R. Maulini, A. Tsekoun, R. Go and C. K. N. Patel, "Tapered 4.7 μm quantum cascade lasers with highly strained active region composition delivering over 4.5 watts of continuous wave optical power," *Optics Express,* vol. 20, no. 4, pp. 4382-4388, 2012.

[16] R. Maulini, A. Lyakh, A. Tsekoun, R. Go, C. Pflügl, L. Diehl, F. Capasso and C. K. N. Patel, "High power thermoelectrically cooled and uncooled quantum cascade lasers with optimized reflectivity facet coatings," *Applied Physics Letters,* vol. 95, p. 141113, 2009.

[17] A. Lyakh, R. Maulini, A. Tsekoun, R. Go, C. Pflügl, L. Diehl, Q. J. Wang, F. Capasso and C. Patel, "3 W continuous-wave room temperature single-facet emission from quantum cascade lasers based on nonresonant extraction design approach," *Applied Physics Letters,* vol. 95, p. 141113, 2009.

[18] M. Semstsiv and W. Masselink, "Above room temperature continuous wave operation of a broad-area quantum-cascade laser," *Applied Physics Letters* , vol. 109, p. 203502, 2016.

[19] B. Jensen, "Quantum theory of the complex dielectric constant of free carriers in polar semiconductors," *IEEE Journal of Quantum Electronics,* vol. 18, p. 1361, 1982.

[20] E. Mujagić, M. Nobile, H. Detz, W. Schrenk, J. Chen, C. Gmachl and G. Strasser, "Ring cavity induced threshold reduction in single-mode surface emitting quantum cascade lasers," *Applied Physics Letters,* vol. 96, p. 031111, 2010.

[21] E. Mujagić, L. K. Hoffmann, S. Schartner, M. Nobile, W. Schrenk, M. P. Semtsiv, M. Wienold, W. T. Masselink and S. G., "Low divergence single-mode surface emitting quantum cascade ring lasers," *Applied Physics Letters,* vol. 93, p. 161101, 2008.

[22] Landau and Lifshitz, The Classical Theory of Fields, Amsterdam: Butterworth Heinemann, 1975.

[23] Y. Bai, S. Tsao1, N. Bandyopadhyay, S. Slivken, Q. Y. Lu, D. Caffey, M. Pushkarsky, T. Day and M. Razeghi, "High power, continuous wave, quantum cascade ring laser," *Applied Physics Letters,* vol. 99, p. 261104, 2011.

[24] E. Mujagic, M. Nobile, D. H., W. Schrenk, J. Chen, C. Gmachl and G. Strasser, "Ring cavity induced threshold reduction in single-mode surface emitting quantum cascade lasers," *Applied Physics Letters,* vol. 96, p. 031111, 2010.

[25] D. H. Chang, T. Azfar, S. K. Kim, H. R. Fetterman, C. Zhang and W. H. Steier, "Vertical adiabatic transition between a silica planar waveguide and an electro-optic polymer fabricated with gray-scalelithography," *Applied Optics,* vol. 38, pp. 2986-2990, 199.

[26] M. Nawrot, L. Zinkiewicz, B. Włodarczyk and P. Wasylczyk, "Transmission phase gratings fabricated with direct laser writing as color filters in the visible," *Optics Express,* vol. 21, p. 31919, 2013.

[27] W. Ren, A. Farooq, D. F. Davidson and R. K. Hanson, "CO concentration and temperature sensor for combustion gases using quantum-cascade laser absorption near 4.7 μm," *Applied Physics B,* vol. 107, p. 849, 2012.

[28] C. Bauer, A. Sharma, U. Willer, J. Burgmeier, B. Braunschweig, W. Schade, S. Blaser, L. Hvozdara, A. Müller and G. Holl, "Potentials and limits of mid-infrared laser spectroscopy for the detection of explosives," *Applied Physics B,* vol. 92, no. 3, p. 327, 2008.

[29] M. C. Phillips and N. Hô, "Infrared hyperspectral imaging using a broadly tunable external cavity quantum cascade laser and microbolometer focal plane array," *Optics Express,* vol. 16, no. 3, p. 1836, 2008.

[30] A. P. M. Michel, P. Q. Liu, J. K. Yeung, P. Corrigan, M. L. Baeck, Z. Wang, T. Day and J. A. Smith, "Quantum cascade laser open-path system for remote sensing of trace gases in Beijing, China," *Optical Engineering,* vol. 49, no. 11, p. 111125, 2010.

[31] A. Kosterev, C. Roller and F. Tittel, "Application of pulsed quantum cascade lasers to NO monitoring in industrial exhaust gases," in *Proceedings of IEEE Sensors 2003*, 2003.

[32] M. Jahjah, W. Ren, P. Stefański, R. Lewicki, J. Zhang, W. Jiang, J. Tarkaab and F. K. Tittel, "A compact QCL based methane and nitrous oxide sensor for environmental and medical applications," *Analyst,* vol. 139, no. 9, p. 2065, 2014.

[33] J. Griffiths, Introduction to Quantum Mechanics, Pearson, 2014.

[34] R. Shankar, Principles of Quantum Mechanics, Springer, 1994.

[35] P. Harrison, Quantum Wells, Wires, and Dots, John Wiley and Sons, 2000.

[36] M. Beck, J. Faist, U. Oesterle, M. Ilegems, E. Gini and H. Melchior, "Buried heterostructure quantum cascade lasers with a large optical cavity waveguide," *Photonics Technology Letters,* vol. 12, p. 1450–1452, 2000.

[37] S. Blaser, D. Yarekha, L. Hvozdara, Y. Bonetti, A. Muller, M. Giovannini and J. Faist, "Room-temperature, continuous-wave, single-mode quantum-cascade lasers at $\lambda \simeq 5.4$ μm," *Applied Physics Letters,* vol. 86, p. 041109, 2005.

[38] A. Evans, S. R. Darvish, S. Slivken, J. Nguyen, Y. Bai and M. Razeghi, "Buried heterostructure quantum cascade lasers with high continuous-wave wall plug efficiency," *Applied Physics Letters,* vol. 91, p. 071101, 2007.

[39] Y. Bai, S. Slivken, S. R. Darvish and M. Razeghi, "Room temperature continuous wave operation of quantum cascade lasers with 12.5% wall plug efficiency," *Applied Physics Letters* , vol. 93, p. 021103, 2008.